Monthly Notices
of the
ROYAL ASTRONOMICAL SOCIETY

Mon. Not. R. Astron. Soc. **418,** 1621–1639 (2011) doi:10.1111/j.1365-2966.2011.19545.x

Interaction of Fanaroff–Riley class II radio jets with a randomly magnetized intracluster medium

M. Huarte-Espinosa,[1,2,3]★ M. Krause[4,5] and P. Alexander[2,3]

[1]*Department of Physics and Astronomy, University of Rochester, 600 Wilson Boulevard, Rochester, NY 14627-0171, USA*
[2]*Astrophysics Group, Cavendish Laboratory, 19 J. J. Thomson Avenue, Cambridge CB3 0HE*
[3]*Kavli Institute for Cosmology, University of Cambridge, Madingley Road, Cambridge CB3 0HA*
[4]*Universitätssternwarte München, Scheinerstr. 1, 81679 München, Germany*
[5]*Max-Planck-Institut für Extraterrestrische Physik, Giessenbachstrasse, 85748 Garching, Germany*

Accepted 2011 July 30. Received 2011 July 27; in original form 2011 May 15

ABSTRACT

A combination of 3D magnetohydrodynamics and synthetic numerical simulations are presented to follow the evolution of a randomly magnetized plasma that models the intracluster medium, under the isolated effects of powerful, light, hypersonic and bipolar Fanaroff–Riley class II jets. We prescribe the cluster magnetic field (CMF) as a Gaussian random field with a Kolmogorov-like energy spectrum. Both the power of the jets and the viewing angle that is used for the synthetic rotation measure (RM) observations are investigated. We find the model radio sources introduce and amplify fluctuations on the RM statistical properties which we analyse as a function of time as well as the viewing angle. The average RM and the RM standard deviation are increased by the action of the jets. Energetics, RM statistics and magnetic power spectral analysis consistently show that the effects also correlate with the jets' power, and that the lightest, fastest jets produce the strongest changes in their environment. We see jets distort and amplify the CMFs especially near the edges of the lobes and the jets' heads. This process leads to a flattening of the RM structure functions at scales comparable to the source size. The edge features we find are similar to ones observed in Hydra A. The results show that jet-produced RM enhancements are more apparent in quasars than in radio galaxies. Globally, jets tend to enhance the RM standard deviation which may lead to overestimations of the CMFs' strength by about 70 per cent. This study means to serve as a pathfinder for the SKA, EVLA and LOFAR to follow the evolution of cosmic magnetic fields.

Key words: MHD – turbulence – methods: numerical – galaxies: active – intergalactic medium – galaxies: jets.

1 INTRODUCTION

Combinations of X-ray and radio observations have revealed the large-scale interactions between radio jets from active galactic nuclei (AGN) and the intracluster medium (ICM; see e.g. Carilli, Perley & Harris 1994; McNamara et al. 2000, 2005; Blanton, Sarazin & McNamara 2003; Nulsen et al. 2005). X-ray surface brightness depressions, or X-ray cavities, are seen in the ICM, the position of which correlates with that of the synchrotron emitting radio galaxy lobes at GHz frequencies, e.g. NGC 1275 in Perseus (Boehringer et al. 1993; Schmidt, Fabian & Sanders 2002), Cygnus A (Carilli et al. 1994; Smith et al. 2002), Hydra A(see Nulsen et al. 2002, and references therein) and several other clusters (Bîrzan et al. 2008). AGN inject large amounts of energy into the ICM in the form of relativistic, magnetized and collimated plasma jets. These seem to be active for periods of some tens of Myr (Alexander & Leahy 1987; Kaiser & Alexander 1999; Krause 2005). The jets drive strong shocks in the ICM which is consequently heated (Binney & Tabor 1995; Kaiser & Alexander 1999; Reynolds, Heinz & Begelman 2001; Alexander 2002; Krause 2003). Jet plasma and magnetic fields inflate a cavity, the 'cocoon', which expands and displaces the ambient medium plasma (Scheuer 1974; Kaiser & Alexander 1997; Heinz, Reynolds & Begelman 1998). The material inside cocoons is responsible the observed radio synchrotron emission.

The interaction between AGN jets and the ICM has been modelled as a hydrodynamical process (Clarke, Harris & Carilli 1997; Kaiser & Alexander 1999; Churazov et al. 2001; Quilis, Bower & Balogh 2001; Alexander 2002; Brüggen & Kaiser 2002; Basson & Alexander 2003; Krause 2005). It is well established however that magnetic fields thread the ICM. Radio polarimetry is the major source of information about cluster magnetic fields (CMFs). The

★E-mail: martinhe@pas.rochester.edu

AGN radio emission is typically ∼10–50 per cent polarized (Bridle & Perley 1984) and the intervening magnetized ICM gives rise to Faraday rotation (see Kim, Kronberg & Tribble 1991, and references therein; for a review see Feretti & Giovannini 2008), which is characterized by the rotation measure (RM). Maps of this quantity have been produced using radio sources located within the ICM or behind it, as well as using cluster radio haloes (for a review, see Carilli & Taylor 2002). The distribution in RM images, along with the assumption that CMFs vary over a single scale, has led to estimates of the strength of CMFs within 5–30 μG in the cool-core clusters Cygnus A, Hydra A, A1795 and 3C 295 (see Dreher, Carilli & Perley 1987; Taylor & Perley 1993; Ge & Owen 1993; Allen et al. 2001, respectively), within 2–8 μG in the non-cool-core clusters Coma, A119, 3C129 (see Feretti et al. 1995, 1999; Taylor et al. 2001, respectively) and also in A2634 and A400 (Eilek & Owen 2002). The RM also suggests that CMFs located in the cores of clusters are stronger than those in their outer regions (Kim et al. 1991; Clarke, Kronberg, Böhringer 2001). A correlation between the RM values and the mass deposition rates of cluster cooling flows has been detected as well (Soker & Sarazin 1990). Observational issues related to Faraday rotation measures of CMFs have been discussed by Rudnick & Blundell (2004).

The structure of CMFs seems to be mainly related to turbulence. This has been inferred using the spatial variation of observed Faraday rotation images and their statistical properties (Tribble 1991; Enßlin & Vogt 2003), in particular, the shape of the RM structure functions (Laing et al. 2008; Guidetti et al. 2010). Murgia et al. (2004) used the RM images of A119 and modelled its magnetic fields with a 3D multiscale tangled geometry. They used spatial variations of the field characterized by a magnetic power spectrum following a power law in Fourier space. Murgia et al. found that both the mean and the standard deviation of the RM, which are used to estimate the strength of CMFs, depend on the magnetic spectral index, n. They conclude that $n \simeq 2$ produces the best fit to the observations in A119. With a similar approach Govoni et al. (2006) reported spectral power-law slope fits of $n \simeq 2$ at the core of A2255, and of $n \simeq 4$ at the outer parts. Also, indexes close to 11/3 have been estimated in A2382 (Guidetti et al. 2008), A400, A2634 and Hydra A (Vogt & Enßlin 2003, 2005).

Models of the evolution of CMFs suggest that the fields' structure is shaped by the dynamics of the ICM via magnetic flux freezing and ideal magnetohydrodynamics (MHD) which is a good approximation in clusters (see Jones 2008, and references therein). In this context, CMFs should follow the ICM advection closely, particularly the one driven by AGN jets. Turbulence in the ICM is expected to be produced during cluster formation and mergers (Ruzmaikin, Sokolov & Shukurov 1989; Roettiger, Stone & Burns 1999; Dolag, Bartelmann & Lesch 2002; Schindler 2002; Dubois & Teyssier 2008; Ryu et al. 2008), as well as by AGN outflows (Enßlin & Vogt 2006; Ruszkowski et al. 2007, and references therein). Turbulent ICM flows are thus believed to amplify CMFs from weak seed fields to the observed microGauss regime by the formation of local small-scale dynamos (see Schekochihin et al. 2004, for a numerical review).

Characteristic depolarization gradients are often observed between the main hotspots of several powerful radio galaxies (see e.g. Laing 1988). Laing (1988) and Garrington et al. (1988) have explained such features using path-length differences between each of the radio lobes and the edge of the observed X-ray emitting ICM that contains them. The RM map of the Fanaroff–Riley class I (FR I; Fanaroff & Riley 1974) radio source Hydra A shows opposite signs in the approaching and the receding radio lobes (Taylor & Perley 1993). Laing et al. (2008) have described these RM fluctuations with synthetic 3D Faraday screens characterized by (i) a random distribution of magnetic fields, (ii) a spherically symmetric gas distribution, (iii) axisymmetric prolate-spheroid cavities resembling the geometry of the Faraday screen projected by Hydra A. These 3D differential Faraday screen models are consistent with the radio source expansion framework of Scheuer (1974), and also with observations of X-ray cavities. The RM gradients in question, therefore, imply that AGN jets make their way by pushing the ICM gas and its magnetic fields at once. This process was recently studied by Guidetti et al. (2011) with high-resolution multifrequency images of Faraday rotation and depolarization of the radio galaxies 0206+35, M 84, 3C 270 and 3C 353. The latter is an extended Fanaroff–Riley class II (FR II) radio source such as the ones that we model in this paper. Guidetti et al. reported, for the first time, well-defined RM bands, with very little small-scale structure, perpendicular to the major axis of the radio lobes of these galaxies. Also, they use a simple time-independent model of both the radio source compression and the ambient medium magnetic fields to generate the RM bands in synthetic observations.

Observations of CMFs are limited by the resolution and sensitivity of telescopes. Many questions about these fields are still open (see Beck, Brunetti & Feretti 2006, for a review). At least for powerful FR II sources there seems to be little mixing of ICM plasma with the synchrotron-emitting one; the observed RM distribution is caused by plasma external to the radio source (Dreher et al. 1987; Carilli & Taylor 2002). The interaction of expanding radio sources with the magnetized ICM should happen locally to the sources. An important question here is how significant this process is when interpreting RM observations as indicators of the properties of both the CMFs and the ICM gas themselves. The SKA (Huarte-Espinosa et al. 2009; Krause et al. 2009), EVLA, e-MERLIN, LOFAR and XEUS (the new generation of telescopes) are planned to have ultra-high sensitivity and sub-arcsecond resolution which will allow a better understanding about the cosmological evolution and structure of CMFs, e.g. we will understand important details about the ICM turbulence (see e.g. Laing et al. 2008; Guidetti et al. 2010) and its heat conduction (see e.g. Schekochihin et al. 2005; Bogdanović et al. 2009).

This is the second of two papers in which we use numerical simulations to study the evolution of magnetic fields in FR II jets and their immediate cluster surroundings. In this work, we introduce a combination of 3D MHD and synthetic RM numerical simulations. We follow the large-scale interaction of powerful radio jets from an FR II radio source with the magnetic fields in the core of a non-cool-core cluster. The structure, the evolution and the polarized synchrotron emission of the radio sources themselves are discussed in our earlier paper (Huarte-Espinosa, Krause & Alexander, 2011, hereafter Paper I). Here we concentrate on the structure of the ICM and the feedback from radio sources. We only follow the evolution of the sources while jets are active. The behaviour of both energetics and magnetic power spectra (in Fourier space) of CMFs is explored as a function of position in the 2D parameter space defined by the velocity and density of the jets. Synthetic RM maps are produced at different viewing angles to investigate the observational signatures of expanding radio sources.

This paper is organized as follows. In Section 2 we briefly describe the formalism of ideal MHD, the numerical methods we use and write about our implementation of the ICM, the CMFs and AGN jets. The results of our simulations are presented in Section 3 along with their interpretation and analysis from the point of view of energetics, RM statistics and magnetic power spectra in Fourier

space. Both the implications and applications of our work are discussed in Section 4. There, we also examine the well-studied case of Hydra A, and finish by commenting about our model assumptions. Finally, in Section 5 we summarize the main results of our work and present our conclusions.

2 SIMULATIONS

2.1 Governing equations

To describe the dynamics of the plasma in the ICM and AGN radio jets, we use the system of non-linear time-dependent hyperbolic equations of ideal compressible MHD. In three dimensions and non-dimensional conservative form, these are given by

$$\frac{\partial \rho}{\partial t} + \nabla \cdot (\rho \boldsymbol{V}) = \dot{\rho}_{\rm j} \tag{1}$$

$$\frac{\partial (\rho \boldsymbol{V})}{\partial t} + \nabla \cdot \left(\rho \boldsymbol{V} V + p + B^2/2 - \boldsymbol{B}\boldsymbol{B}\right) = \rho \boldsymbol{g} + \dot{\boldsymbol{P}}_{\rm j} \tag{2}$$

$$\frac{\partial E}{\partial t} + \nabla \cdot \left[\left(E + p + B^2/2\right)\boldsymbol{V} - \boldsymbol{B}(\boldsymbol{V}\cdot\boldsymbol{B})\right] = \dot{E}_{\rm j} \tag{3}$$

$$\frac{\partial \boldsymbol{B}}{\partial t} - \nabla \times (\boldsymbol{V} \times \boldsymbol{B}) = 0, \tag{4}$$

where ρ, p, $\boldsymbol{V}$ and $\boldsymbol{B}$ are the plasma density, thermal pressure, flow velocity and magnetic fields, respectively. In (3), $E = p/(\gamma - 1) + \rho V^2/2 + B^2/2$ and is the total energy density, while γ is the ratio of specific heats. In the right-hand side of (1), (2) and (3), we have source terms to implement jets via the injection of mass, $\dot{\rho}_{\rm j}$, momentum, $\dot{P}_{\rm j}$, and kinetic energy, $\dot{E}_{\rm j}$ (see Section 2.4), as well as a Newtonian gravitational acceleration, $\boldsymbol{g}$, in order to keep the initial plasma in a magnetohydrostatic equilibrium.

2.2 Code and implementation

We solve the equations of ideal MHD in three dimensions using the numerical code FLASH 3.1 (Fryxell et al. 2000). FLASH's new multidimensional unsplit constrained transport solver is employed to maintain the divergence of magnetic fields down to $\lesssim 10^{-12}$ (Lee & Deane 2008). A diffusive HLLC solver (Batten et al. 1997) prevents spurious low pressure and density values from appearing in the grid. We use a Courant–Friedrichs–Lewy parameter of 0.25 and periodic boundary conditions in all the domains' faces. These boundary conditions prevent numerical noise from polluting the magnetic spectrum in the grid (Section 2.3.1). Our computational domain is a cube with edges $|\boldsymbol{x}| \leq 1/2$ computational units (which represent a volume of 200 kpc^3), Cartesian coordinates and a uniform grid with 200^3 cells.

We present six simulations to study the effects of active AGN jets on the magnetic fields in the core of a non-cool-core cluster. Five simulations, which we refer to as *jets-simulations*, are designed to experiment with the power of the jets. We do this by varying their velocities and densities. These jet-simulations are the same that we present in Paper I. The other simulation, the *no-jets* model, is carried out in order to follow the evolution of the ICM plasma without any perturbations throughout the same simulation time-steps as the jet-simulations. All of these models are labelled descriptively and summarized in Table 1. See Paper I for a discussion about the low densities and hypersonic velocities of the jets.

Table 1. Simulations and parameters.

Simulation name	$v_{\rm j}$ [a] (Mach)	η [b]	$L_{\rm j}$ [c] ($\times 10^{38}$ W)	$t_{\rm e}$ [d] (Myr)
Lighter-slow	40	0.004	4.6	14.1
Light-slow	40	0.020	17.2	8.3
Lighter-fast	80	0.004	28.1	7.1
Light-fast	80	0.020	128.8	4.4
Lighter-faster	130	0.004	112.8	4.7
No-jets	–	–	–	All of the above

[a]Time-averaged jets velocity in the nozzle. It is equal to the external Mach number.
[b]Time-averaged jets versus ambient density contrast in the nozzle.
[c]Jets power from equation (11) in Paper I.
[d]Simulations' ending times.

2.3 Initial conditions

We implement the cluster gas using an ideal gas equation of state, a King density profile (King 1972) and a state of magnetohydrostatic equilibrium with a background Newtonian central gravity field (see Paper I, for details).

2.3.1 Cluster magnetic fields

The magnetic field within the cluster is set up as an isotropic random field with a power-law energy spectrum. Following Tribble (1991) and Murgia et al. (2004), we generate a cubic grid in Fourier space. For each cell, we define three components of a vector potential which takes the form $\tilde{\boldsymbol{A}}(\boldsymbol{k}) = \boldsymbol{A}(\boldsymbol{k})e^{i\boldsymbol{\theta}(\boldsymbol{k})}$, where $\boldsymbol{k}$ is the frequency vector ($k^2 = k_x^2 + k_y^2 + k_z^2$) and 'i' is the unitary complex number, while $\boldsymbol{A}$ and $\boldsymbol{\theta}$ are the vector's amplitudes and phases, respectively. We draw $\boldsymbol{\theta}(\boldsymbol{k})$ from a uniform random distribution within 0 and 2π, and $\boldsymbol{A}(\boldsymbol{k})$ is also randomly distributed but has a Rayleigh probability distribution:

$$P(A,\theta)\,{\rm d}A{\rm d}\theta = \frac{A}{2\pi|A_k|^2}\exp\left(-\frac{A^2}{2|A_k|^2}\right){\rm d}A{\rm d}\theta, \tag{5}$$

where we choose the power law ansatz

$$|A_k|^2 \propto k^{-\zeta}, \tag{6}$$

for a given slope ζ.

We transform to real space by taking the inverse fast Fourier Transform (Press et al. 1992) of $\tilde{\boldsymbol{A}}(\boldsymbol{k})$. The resulting magnetic vector potential $\boldsymbol{A}(\boldsymbol{x})$ is multiplied by the plasma density radial profile (see Paper I, section 2.3.1). This multiplication implements the magnetic flux freezing by generating magnetic fields, the strength of which follows the plasma density and pressure profiles.

We then take the curl of this vector to get the magnetic field which is normalized so that the ICM thermal pressure is approximately 10 times larger than its magnetic pressure, i.e.

$$\beta_{\rm m} = \frac{p}{\boldsymbol{B}^2/2} \sim 10, \tag{7}$$

which is a reasonable value in this context (Carilli & Taylor 2002).

This procedure yields solenoidal magnetic fields which are tangled at scales of the order of our computational resolution, and characterized by spatial variations that follow a magnetic power spectrum with a power law of the form:

$$|B|^2 \propto k^{-\zeta+2} = k^{-n}. \tag{8}$$

We choose a Kolmogorov-like 3D turbulent slope $n = -11/3$, based on the work of Vogt & Enßlin (2003, 2005) and Guidetti et al. (2008). Note that other values for n would also have been possible (cf. Section 1, above). This choice may also be motivated by theoretical studies of the cosmological evolution of CMFs (e.g. Brüggen et al. 2005; Ryu et al. 2008; but compare also with Schekochihin et al. 2004; Xu et al. 2010). The topology of these fields is (of course) constrained by the approximation of ideal MHD and thus we do not model physical magnetic reconnection, but the simulations do present numerical resistivity. We note that the Fourier method implicitly imposes maximum and minimum scales.

2.4 Jets

By implementing source terms to the equations (1), (2) and (3), we inject mass, momentum and kinetic energy to the central grid cells located within a control cylinder of radius, r_j, and height, h_j, which are resolved by three and eight cells, respectively. Inside this 'nozzle' we update the plasma density and x-velocity using the constant source terms $\dot{\rho}_j$ and $\dot{v}_j$.

Bipolar back-to-back jets are continuously injected until they reach the computational boundaries. The simulations are stopped at this point. The nozzle plasma pressure, p_j, takes the constant value of the central ambient pressure (i.e. ρ_c/γ), while $\boldsymbol{B}$, v_y, v_z and E evolve according to the MHD equations (1)–(4). This implementation is similar to that of Omma et al. (2004), but generalized here to the MHD case.

The power of the jets is given in Table 1 and computed using the equation (11) in Paper I.

2.4.1 Cocoon contact surface

We implement a passive tracer, $\tau(\boldsymbol{x}, t)$, which is injected along with the jets' plasma to distinguish it from the one of the ambient medium. Defined as a real number within $(1 \times 10^{-10}, 0.99)$, τ initially takes these extreme values in the ICM and in the jets' nozzle, respectively. The tracer is advected with the jets, and a comparison of the distribution of both τ and ρ allows us to identify the contact surface of the cocoon with an accuracy of about four computational cells.

3 RESULTS AND ANALYSIS

To analyse our simulations in the context of galaxy cluster cores, we scale the plasma variables in the following way. The size of the computational domain is given by $L = 200$ kpc, the ICM speed of sound as $c_s = 1.66 \times 10^3\,\mathrm{km\,s^{-1}}$ – which corresponds to a temperature of 10^8 K – and the cluster central density as $\rho_c = 1 \times 10^{-23}\,\mathrm{kg\,m^{-3}}$. Each computational cell is 1 kpc long, the central cluster radius is $r_c = 160$ kpc and the nozzle's radius and height take the values $r_j = 3$ kpc and $h_j = 8$ kpc, respectively. For the given ICM properties, the initial rms magnetic field is $\sim$20 μG.

3.1 Evolution of the plasma

We let the magnetized ICM plasma described in Section 2.3 to relax for $\sim$118 Myr before we inject the jets. This time-scale represents one thermal crossing time (i.e. the ratio of the computational domain's length over the gas sound speed). During this phase the magnetic energy of the cluster dominates the kinetic energy which was initially zero. CMFs produce local, subsonic and homogeneous random motion on the plasma. We see the 3D magnetic power spectrum of the plasma preserves the initial Kolmogorov turbulent profile. Mild losses of about half an order of magnitude develop in the spectrum at scales $\lesssim 10$ kpc due to numerical diffusion. We only follow this phase in order to reduce the initial differences between the magnetic and the thermal pressure profiles of our initial setup (Section 2.3), but we do not intend to simulate the evolution of the ICM and its magnetic fields at any time before the injection of our jets.

The left column in Fig. 1 shows the ICM plasma at the end of the relaxation phase. These are logarithmic false colour maps of the plasma density (top row), the magnetic field strength (middle row) and the magnetic beta parameter (bottom row). The injection of the jets starts at this point; at $t_{jet} = 0$ Myr. Then we see that our simulations produce the basic fluid dynamical structures found in previous jet simulations (e.g. see Reynolds, Heinz & Begelman 2001; Basson & Alexander 2003; Omma et al. 2004; Krause 2005). A strong bow shock is formed in the ambient medium, behind which a contact discontinuity bounds the cocoon inflated by the jets' former plasma and magnetic fields. The middle column in Fig. 1 shows the plasma after the effects of the light-slow source at the end of that simulation. In the right column, we present the plasma after the injection of the lighter-faster source at the end of that simulation (see Table 1). Note the dependence of the cocoon geometry, which is marked by yellow surfaces in Figs 1(b) and (c), on the density of the jets. A full discussion of the source properties and evolution is covered in Paper I.

As the sources develop, the ambient plasma is compressed and the shocked region between the cocoons and the bow shocks expands. During this process, the CMF component that is normal to the direction of the cocoon expansion is compressed and stretched (Fig. 2). The strength of the CMFs is thus amplified, particularly ahead of the jets' working surfaces, and shows local enhancements above the mean field intensity – Figs 1(e) and (f). Such enhancements reach factors up to about 7.4, 7.7, 10.9, 7.5 and 12.2, respectively, for the jet-simulations in the order in which they appear in Table 1.

We see (Fig. 1, bottom row) that jets produce considerable gradients in β_m inside the sources; the cocoons and the ambient medium show values of order 10 000 and 10, respectively. Yet the global change of β_m in the ambient medium is fairly low, $\beta_m \sim 10$ throughout the simulations.

3.2 Energetics

We have calculated the energetics of the ICM as a function of the source size which is measured from hotspot to hotspot. Fig. 3 has three panels which show the thermal, kinetic and magnetic energies of the ICM, from top to bottom. Each panel has six profiles corresponding to the simulations in Table 1. We see that in the absence of jets (black dotted curve) the ICM thermal energy increases slightly in time due to dissipation of magnetic energy which falls by $\sim$10 per cent due to numerical diffusion. When jets are present, on the other hand, the total energy of the ICM increases consistently. The energy transfer from jets to the ambient medium is predominantly thermal and proportional to their velocity. Jets with a density contrast of 4×10^{-3} are more efficient in this process than those with a density contrast of 2×10^{-2} (Fig. 3). This behaviour is characteristic of very light jets which inflate fat cocoons that provide large areas over which to affect the surrounding ICM. In contrast, the forward momentum of relatively heavier jets leads to smaller cocoons. Also, both the pressure and the speed of sound inside the cocoons with

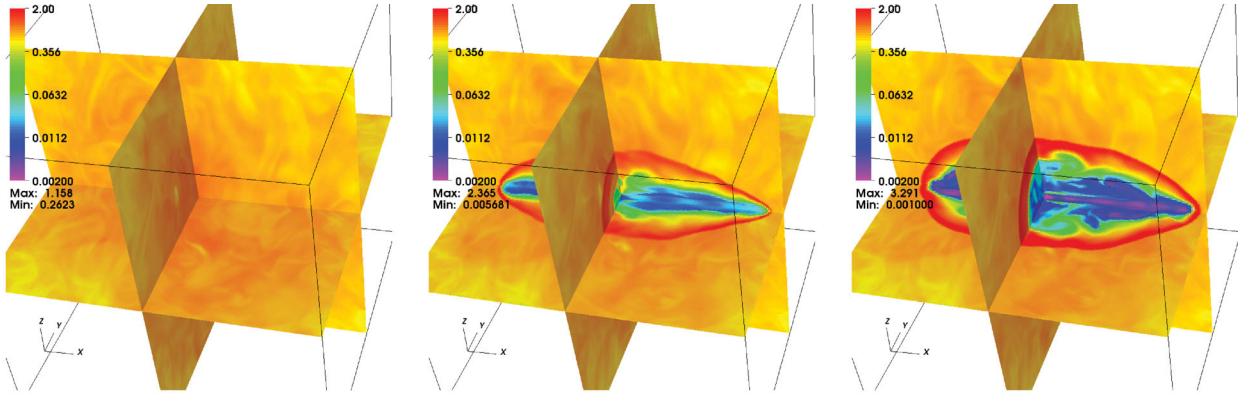

(a) $log(\rho_{ICM})$, $t_{jet} = 0$ Myr

(b) $log(\rho_{ICM})$, Mach= 40, $\eta = 0.02$ & $t_{jet} = 8.3$ Myr

(c) $log(\rho_{ICM})$, Mach= 130, $\eta = 0.004$ & $t_{jet} = 4.7$ Myr

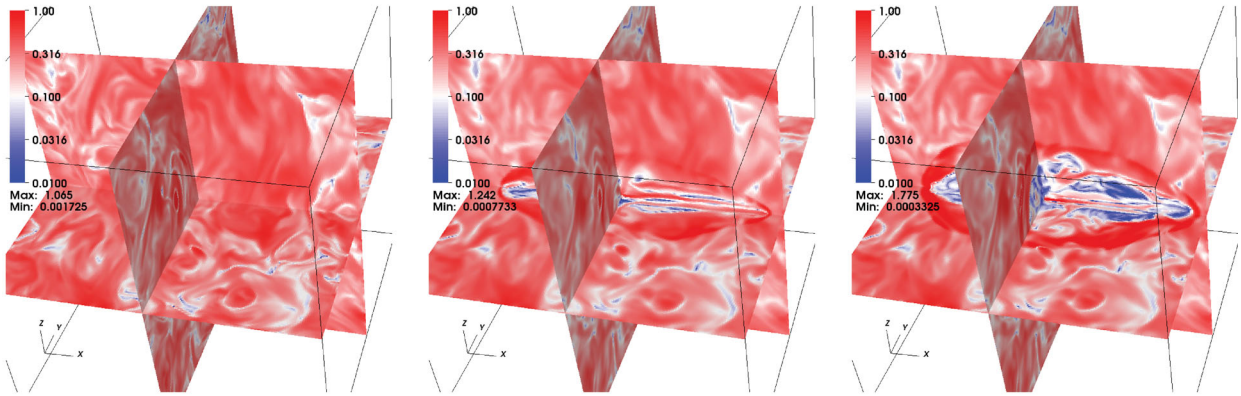

(d) $log(|B|^2)$, $t_{jet} = 0$ Myr

(e) $log(|B|^2)$, Mach= 40, $\eta = 0.02$ & $t_{jet} = 8.3$ Myr

(f) $log(|B|^2)$, Mach= 130, $\eta = 0.004$ & $t_{jet} = 4.7$ Myr

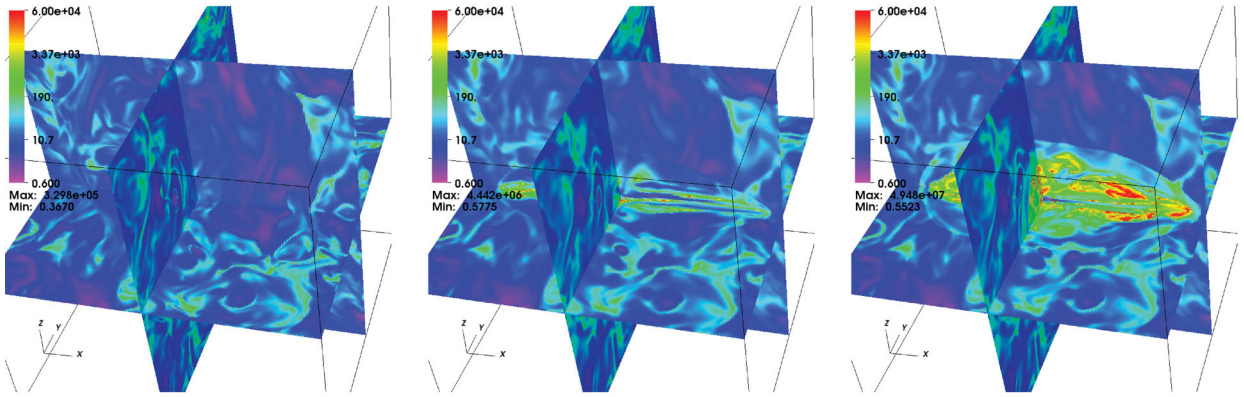

(g) $log(\beta_m)$, $t_{jet} = 0$ Myr

(h) $log(\beta_m)$, Mach= 40, $\eta = 0.02$ & $t_{jet} = 8.3$ Myr

(i) $log(\beta_m)$,Mach= 130, $\eta = 0.004$ & $t_{jet} = 4.7$ Myr

Figure 1. Logarithmic false colour maps of the plasma density (top row), the magnetic fields strength (middle row) and the magnetic beta parameter (bottom row). The top and middle rows are shown in computational units. The left column shows the ambient plasma after one relaxation time (equivalent to 118.5 Myr), but just before the injection of jets. The middle column shows the plasma after the effects of the light-slow source at the end of the simulation. The right column shows the ambient medium after the injection of the lighter-faster source at the end of the simulation.

lighter jets are higher than those inside the cocoons with relatively heavier jets (Krause 2003).

The decay of the ICM magnetic energy is slowed down, but not suppressed, by the Mach-40 jets (see the green and dark-blue curves in Fig. 3). In contrast, the faster jets are able to significantly impede the decay by the time their cocoons extend for ∼70 kpc (from hotspot to hotspot). As the lightest, faster sources continue expanding (see the red and light-blue curves) they increase the

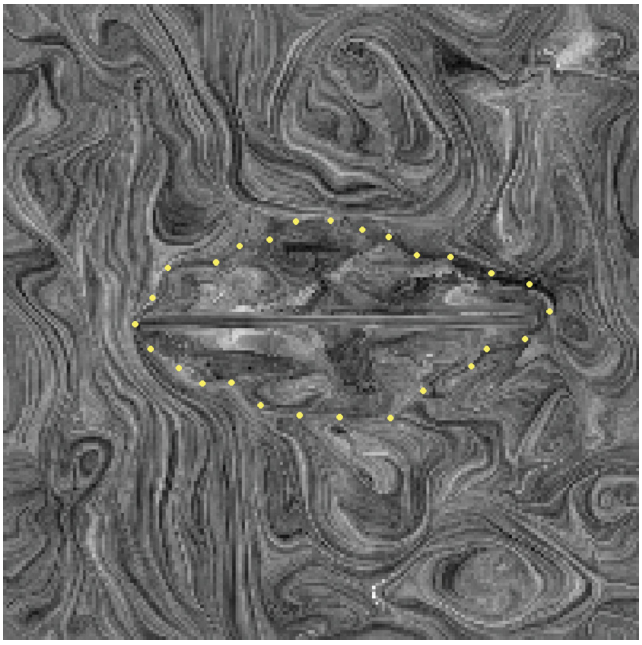

Figure 2. Central slice through our cubic computational domain showing the geometry of CMF lines under the effects of the 'lighter-fast' source at $t_{\rm jet} = 5.3$ Myr. The cocoon is marked with yellow dots and jets are in the plane of the image, horizontally. We note the grey-scale has no relation to the strength of the fields at all.

energy of the CMFs in proportion to the jet velocity. This increase however tends to flatten modestly after the cocoons of these sources are ∼130 kpc long.

3.3 Rotation measure

We use the information from our simulations to produce synthetic RM maps and compare the predictions of our models with the observations. Our maps are produced by computing

$$\mathrm{RM} = 812 \int_{D_0/\mathrm{kpc}}^{D/\mathrm{kpc}} \left(\frac{n_\mathrm{e}}{\mathrm{cm}^{-3}}\right) \left(\frac{B_\parallel}{\mu\mathrm{G}}\right) \mathrm{d}l \ \mathrm{rad\,m}^{-2}, \qquad (9)$$

along the line of sight, where D_0, D, n_e and $B_\parallel$ are the location of the computational domain's boundary, the location of the cocoon's contact surface (the spatial distribution of which is given by the tracer of the jets; Section 2.4.1), the ICM electron density and the CMF component that is parallel to the line of sight, respectively. We note that the magnetic fields inside the sources are not considered for this analysis, and hence there is no internal rotation.

The viewing or inclination angle, θ_v, is measured from the jets' axis to the line of sight. Jets point towards the observer when $\theta_\mathrm{v} = 0°$, and higher viewing angles are obtained by rotating the simulation data cubes perpendicularly to the jets, anticlockwise. Thus jets are on the plane of the sky, horizontally, at $\theta_\mathrm{v} = 90°$. For a consistent comparison at all viewing angles, the computational cells which are located at radii larger than 100 kpc are discarded from our cubic computational domain of 200 kpc^3 (Fig. 4). The geometry of the Faraday screens, or the RM integration volumes, depends on both the shape of the cocoons' contact surface – which is different in each simulation – and the viewing angle. Observationally, the measured screens are modified by noise and the finite telescope resolution as well (Enßlin & Vogt 2003).

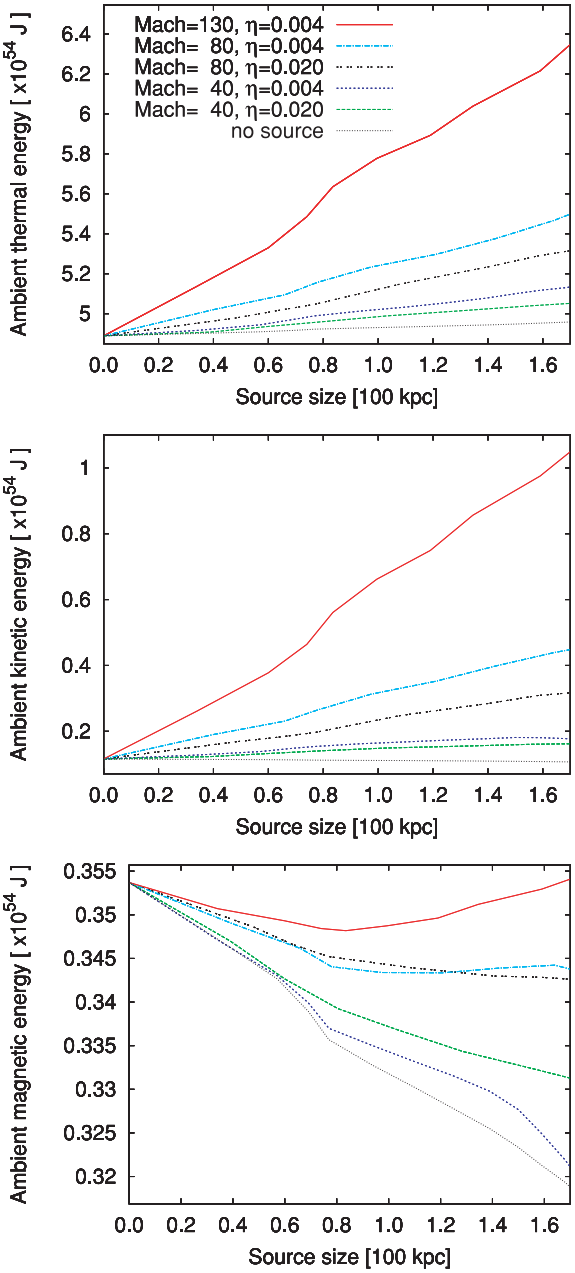

Figure 3. ICM energetics as a function of source size measured from hotspot to hotspot.

3.3.1 *No-source RM maps*

We are only interested in the statistical changes of the RM which are caused by the expansion of FR II sources. In our simulations, however, we also see modest, yet detectable, RM variations that are caused by subsonic random flow in the ICM, independently of the source expansion (see top of Section 3.1). In order to interpret the mechanical work specifically done by the sources on the ICM's gas and magnetic fields, we produce *'no-source'* RM maps. To this end, we use equation (9), but combine information from different simulations in the following way:

(i) n_e and $B_\parallel$ are taken from the no-jets simulation (Section 2.2) and

(ii) D_0 and D, which define the geometry of the Faraday screen, are taken from the jets-simulations (see Table 1).

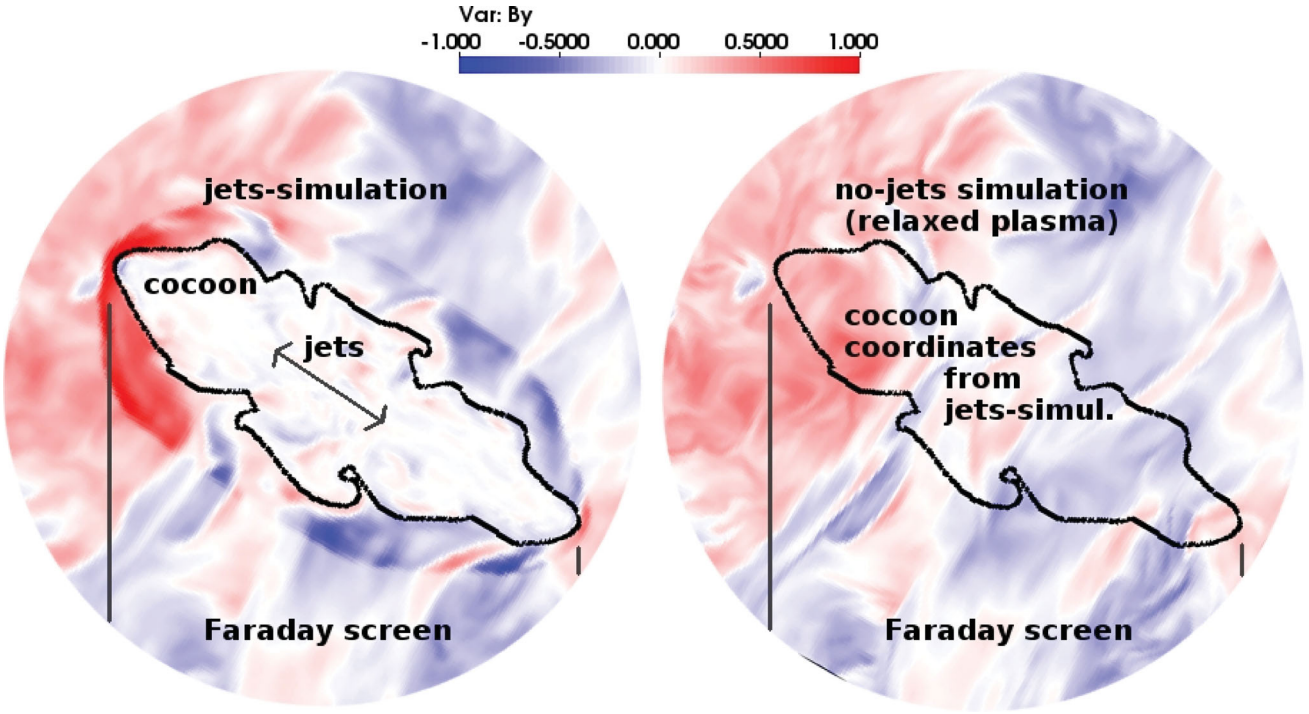

Figure 4. Sketch of the geometry employed for the no-source RM maps. The linear colour scale shows the y-component of the CMFs normalized to their maximum value in the X–Z plane through the centre of the cubic computational domain. No-source RM images are produced using equation (9); gas density and magnetic field factors are taken from the no-jets simulation, whereas the integration limits are taken from a jets-simulation. See Section 3.3.1 for details.

This idea is illustrated in Fig. 4. Hence 'no-source' RM maps give the RM structure which would have been observed against an evolving radio source had it *not* affected the ICM dynamically.

We have produced no-source RM maps at $t_{\rm jet} = 0$, 4.4, 4.7, 7.1, 8.3 and 14.1 Myr (i.e. just before the injection of jets and at the five time-steps that correspond to the end of the jets-simulation, $t_{\rm e}$; see Table 1).

3.3.2 Synthetic RM maps

Figs 5–10 show our synthetic RM maps and their histograms. Each figure corresponds to one of the jets-simulations and a viewing angle (either 45° or 90°). Panels are arranged by rows. The top row (a) shows (from left to right): the no-source RM map at $t_{\rm jet} = 0$ Myr (using the cocoon coordinates of the corresponding source at $t_{\rm jet} = t_{\rm e}$); the no-source RM map at $t_{\rm jet} = t_{\rm e}$ (also using the cocoon coordinates of the corresponding source at $t_{\rm jet} = t_{\rm e}$); the RM map at $t_{\rm jet} = t_{\rm e}$. The middle row, (b), has panels in which the black, the red and the green profiles correspond to horizontal lines through the left, the middle and the right maps in the top row, respectively. The middle panel in row (b) shows 1D RM profiles at $y = 0$ kpc. The left- and right-hand panels in (b) show 1D RM profiles at symmetric y-values with respect to $y = 0$ kpc, which go near the sources' edge. Finally, the bottom row, (c), shows histograms of the three maps in the top row – where (again) the black, the red and the green profiles in (c) correspond to the left, the middle and the right maps in (a), respectively.

Our synthetic RM maps consistently show that powerful jets enhance the RM distribution locally. We see this process scales with both the jet velocity and density. More spherical cocoons, such as those that are typically shown by very light jets, generally yield higher RM values; they favour the alignment of enhanced magnetic field components with the line of sight.

The considered RM enhancement occurs because the expanding hypersonic sources compress the ICM gas and magnetic fields in the shocked ambient region which is located just ahead of the cocoons' contact surface. Magnetic field lines are compressed and stretched perpendicularly to the source expansion direction (Fig. 2). We see that this RM increase is typically larger at the sources' edge, where the alignment between the line of sight and the compressed CMF lines is more important. Moreover, shocks are stronger near the hotspots than near the sides of the cocoons. Such structure is also evident in the RM maps – e.g. see the 'lighter-faster' source map, Fig. 8(a), right-hand panel.

By comparing the top-left and top-middle panels in Figs 5–10, as well as the black and the red profiles in the rows (b) and (c), we see a modest RM variation in the 'no-source' RM maps. Relative to such small changes, the source-produced RM enhancements are larger, particularly those of the jets with velocities exceeding Mach 80. The 'no-source' RM maps produced at $\theta_{\rm v} = 45°$ show the expected global asymmetry: having a shorter total Faraday depth, the approaching source lobes consistently show lower RM values and variation than the receding lobes. We see powerful radio jets enhance these RM gradients and that the histograms in panel (c) of Figs 5–10 show that this effect happens at the highest RM values. When jets are on the plane of the sky ($\theta_{\rm v} = 90°$) the RM histograms tend to be double peaked. Yet at $\theta_{\rm v} = 45°$, the histograms are narrower and single peaked; the Faraday depth is more uniform at $\theta_{\rm v} = 90°$. Further, the alignment of the compressed CMF components with the line of sight is more important for observations at angles within 20°–70° due to the prolate spheroid geometry of cocoons. Therefore, we see higher RM values at 45° than at 90°. The choice of 45° is interesting because it separates quasars from radio galaxies in the unification model of Barthel (1989).

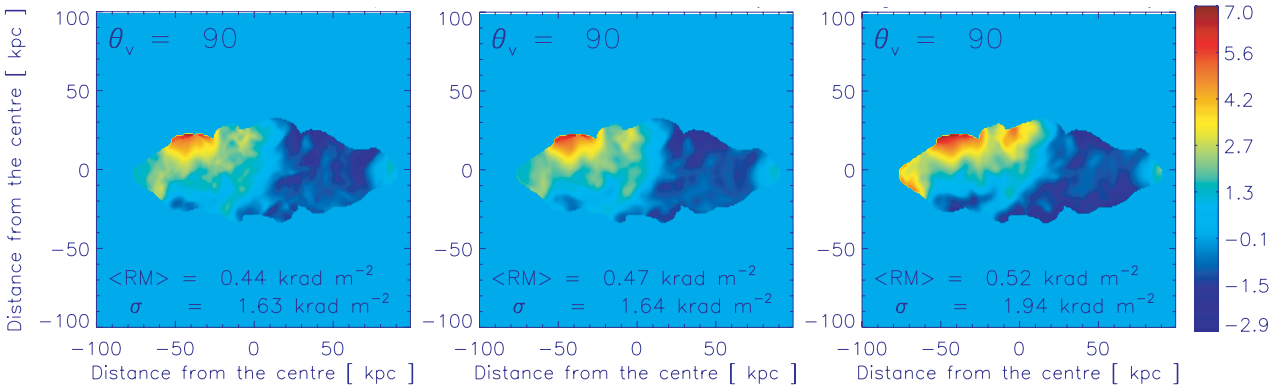

(a) No-source RM map at $t = 0$ Myr (left), No-source RM map at $t = 7.1$ Myr (middle), RM map at $t = 7.1$ Myr (right).

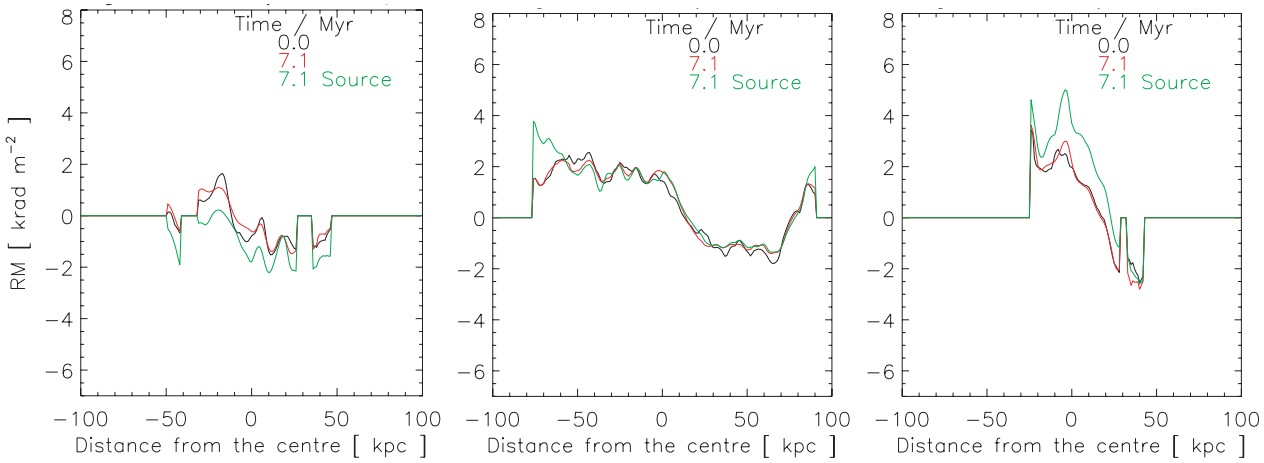

(b) RM at $y = -25$ (left), $y = 0$ (middle) and $y = 25$ kpc (right). The black, red and green curves correspond to the left, the middle and the right panels in (a), respectively.

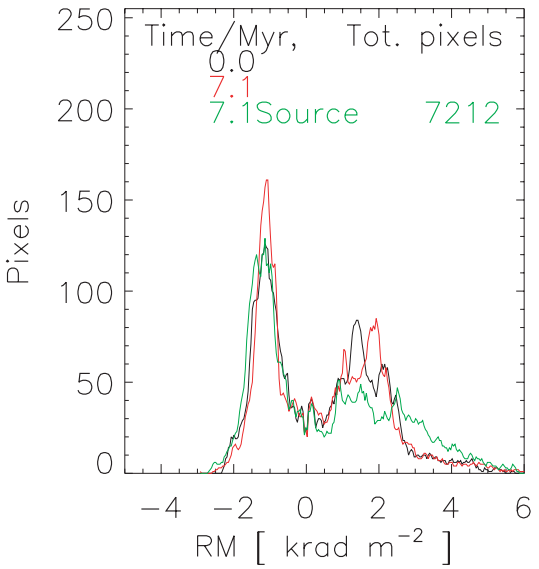

(c) RM histograms of the three maps in (a). Colors are as in panel (b).

Figure 5. RM maps and histograms of the lighter-fast simulation at $\theta_v = 90°$. (a) From left to right: the no-source RM map at $t_{jet} = 0$ Myr (using the cocoon coordinates of the lighter-fast source at $t_{jet} = 7.1$ Myr); the no-source RM map at $t_{jet} = 7.1$ Myr; the RM map at $t_{jet} = 7.1$ Myr. (b) Each panel shows RM profiles corresponding to horizontal lines through the three maps in (a).

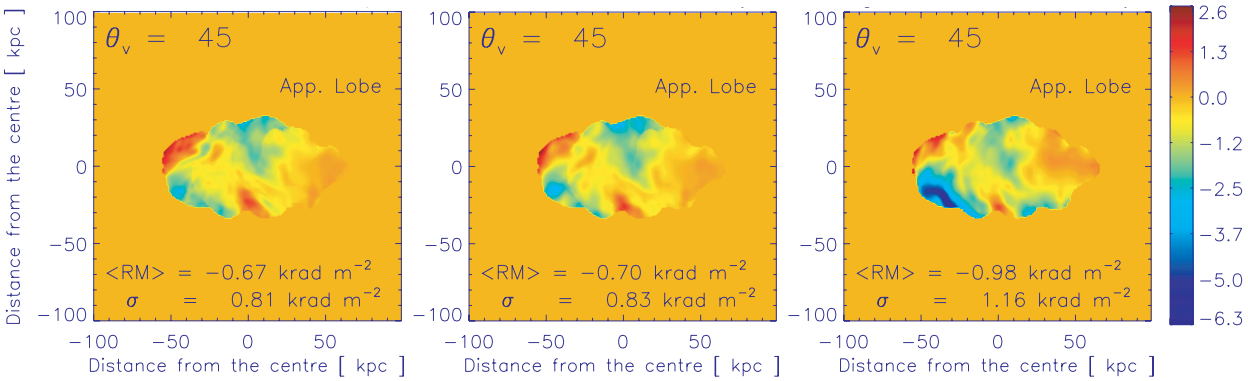

(a) No-source RM map at $t = 0$ Myr (left), No-source RM map at $t = 7.1$ Myr (middle), RM map at $t = 7.1$ Myr (right).

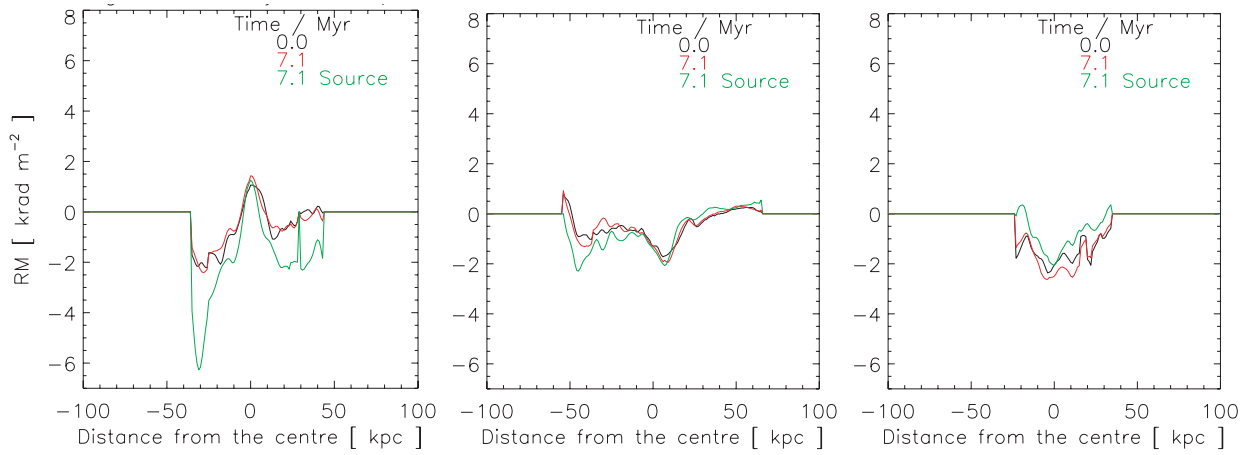

(b) RM at $y = -25$ (left), $y = 0$ (middle) and $y = 25$ kpc (right). The black, red and green curves correspond to the left, the middle and the right panels in (a), respectively.

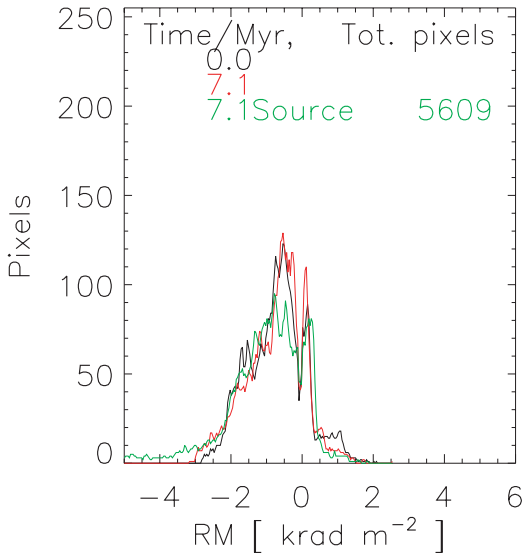

(c) RM histograms of the three maps in (a). Colors are as in panel (b).

Figure 6. Same as Fig. 5 but for $\theta_v = 45°$. The approaching lobe is on the positive distance range.

3.3.3 RM evolution

The time evolution of the RM statistics has been followed as the sources expand. In Fig. 11 the top row displays the evolution of the mean RM. The bottom row shows the evolution of the RM standard deviation. The viewing angle is 45° and 90° for the left and right columns, respectively. RM maps are produced using expanding sources at corresponding time-steps. Profiles are normalized to their corresponding initial values (i.e. to either the mean RM or the RM standard deviation produced against Faraday screens of matching

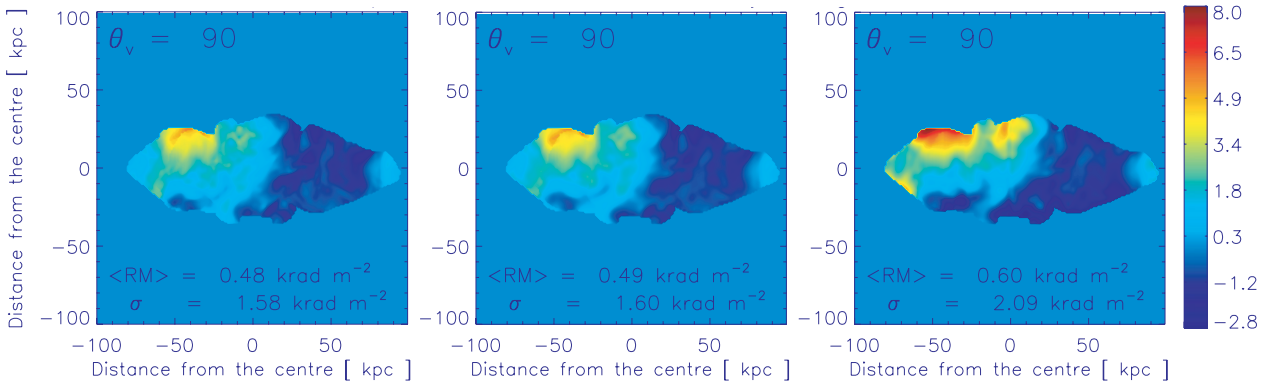

(a) No-source RM map at $t = 0$ Myr (left), No-source RM map at $t = 4.7$ Myr (middle), RM map at $t = 4.7$ Myr (right).

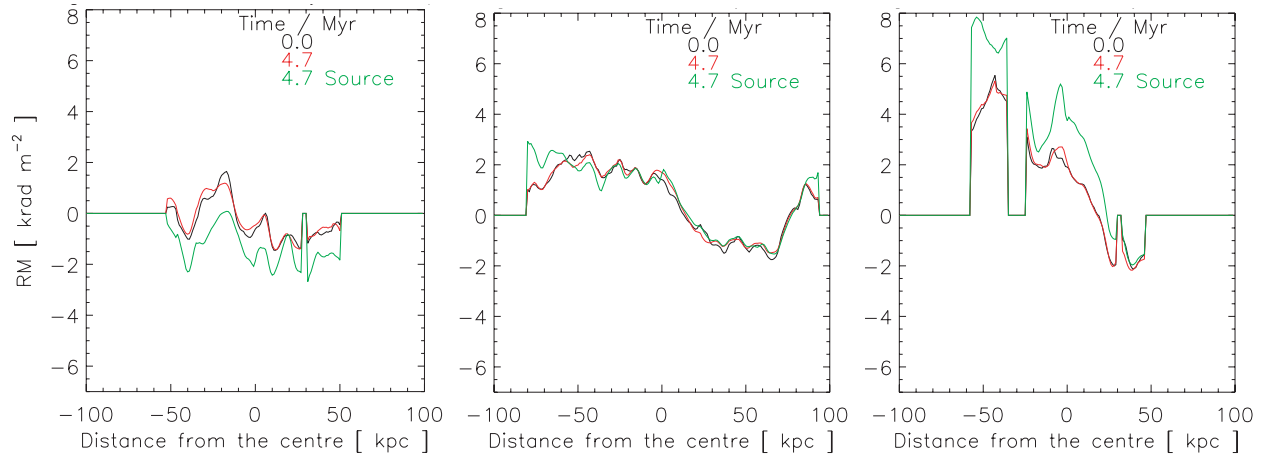

(b) RM at $y = -25$ (left), $y = 0$ (middle) and $y = 25$ kpc (right). The black, red and green curves correspond to the left, the middle and the right panels in (a), respectively.

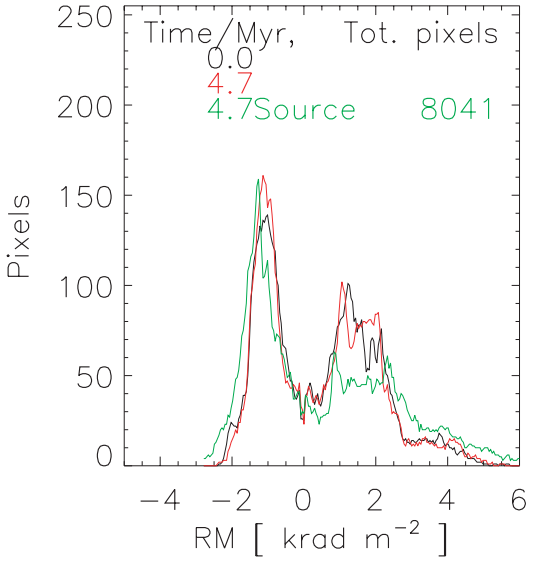

(c) RM histograms of the three maps in (a). Colors are as in panel (b).

Figure 7. Same as Fig. 5 but for the lighter-faster jets.

sources, but on the gas and magnetic field distribution at $t_{\rm jet} = 0$; see Section 3.3.1).

As the sources expand, we see the RM statistics scale up with the speed of the jets. Generally, the 'lighter' sources yield more important changes on the statistics than the 'light' sources, by factors of about 2–7. We see the gradients in the RM statistics evolution profiles (Fig. 11) follow similar trends to those of the ICM energetics profiles (Fig. 3). Also, in agreement with the RM histograms

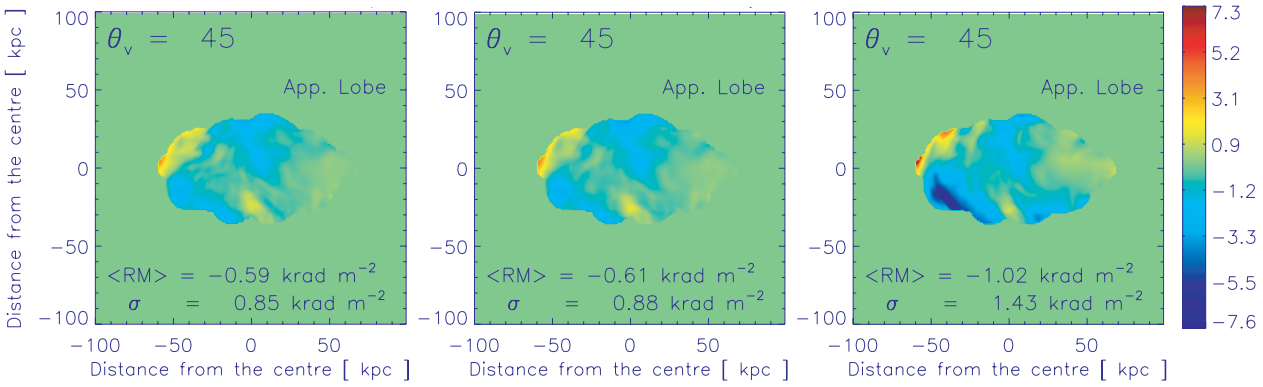

(a) No-source RM map at $t = 0$ Myr (left), No-source RM map at $t = 4.7$ Myr (middle), RM map at $t = 4.7$ Myr (right).

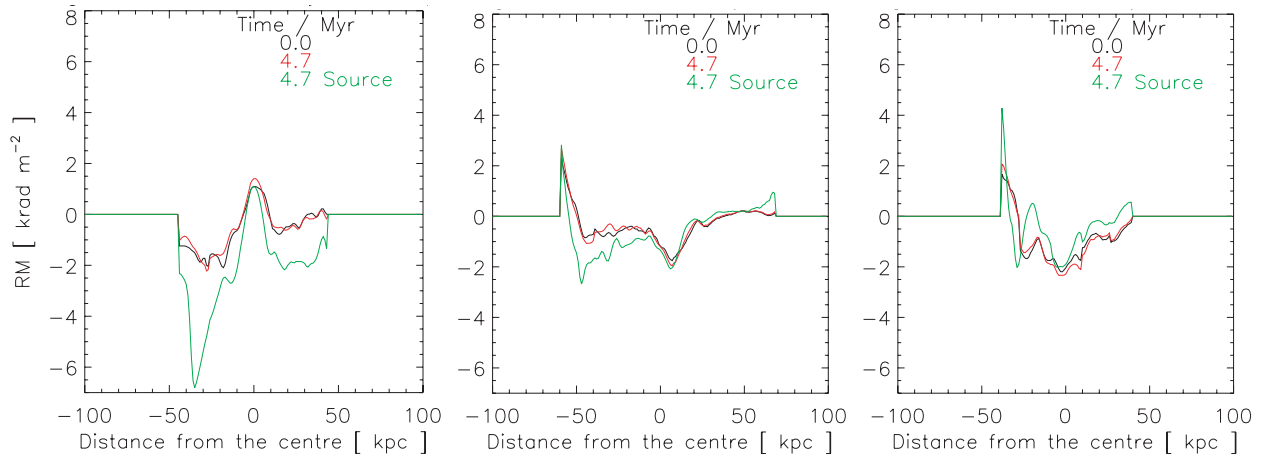

(b) RM at $y = -25$ (left), $y = 0$ (middle) and $y = 25$ kpc (right). The black, red and green curves correspond to the left, the middle and the right panels in (a), respectively.

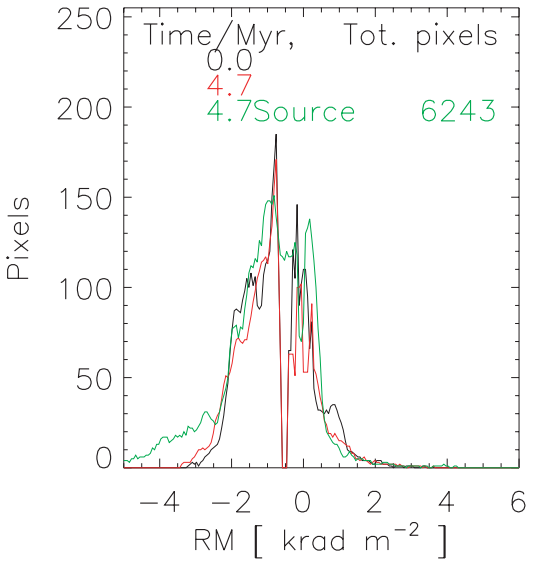

(c) RM histograms of the three maps in (a). Colors are as in panel (b).

Figure 8. Same as Fig. 5 but for the lighter-faster jets and $\theta_v = 45°$. The approaching lobe is on the positive distance range.

(panel c, Figs 5–10), the effect of the sources on the RM evolution appears to be more significant for observations made at 45° than at 90°. This is, again (see previous section), caused by the geometry of cocoons.

Gradients in the RM statistics evolution profiles (Fig. 11) also show a relation with those in the pressure evolution profiles that we have shown in Fig. 12. The latter show that the 'slow' sources reach pressure equilibrium with the ambient medium earlier than

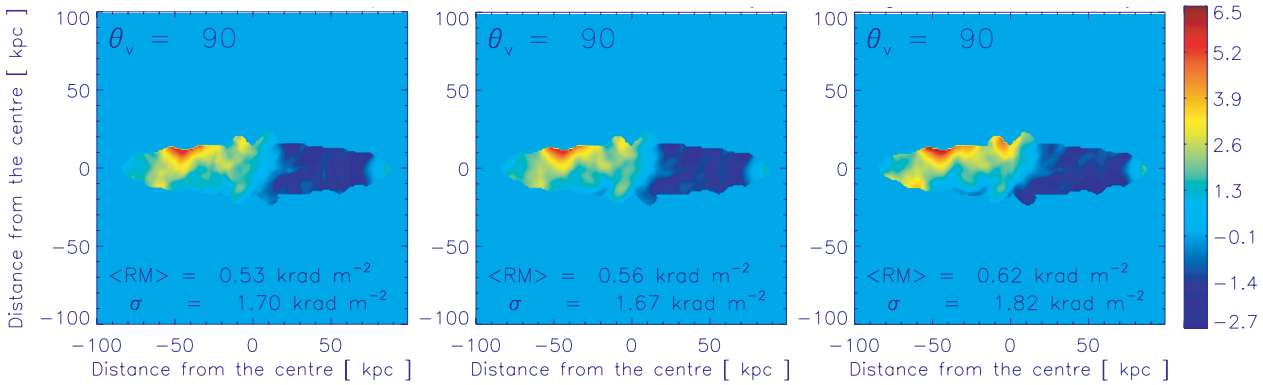

(a) No-source RM map at $t = 0$ Myr (left), No-source RM map at $t = 4.5$ Myr (middle), RM map at $t = 4.4$ Myr (right).

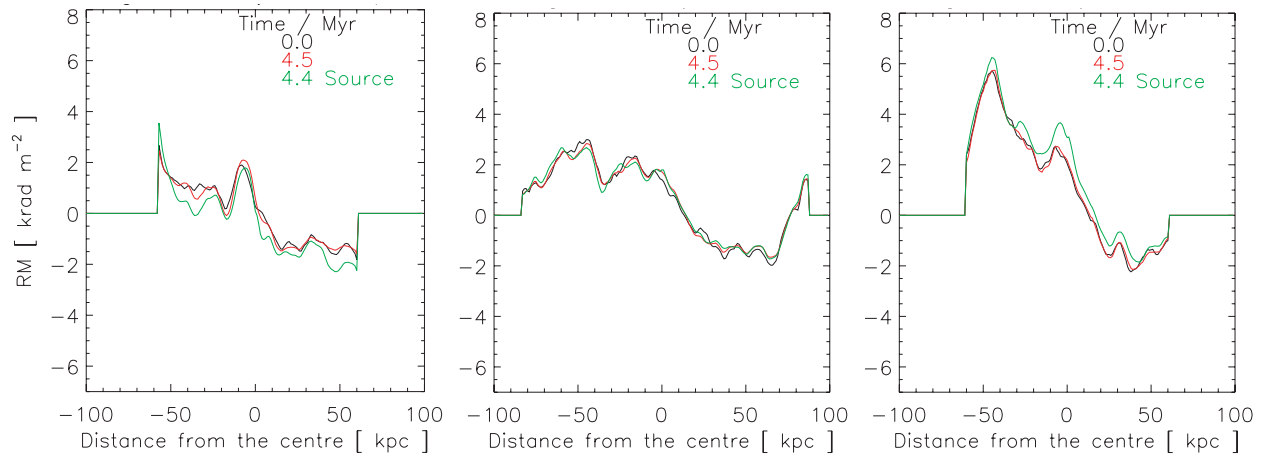

(b) RM at $y = -12$ (left), $y = 0$ (middle) and $y = 12$ kpc (right). The black, red and green curves correspond to the left, the middle and the right panels in (a), respectively.

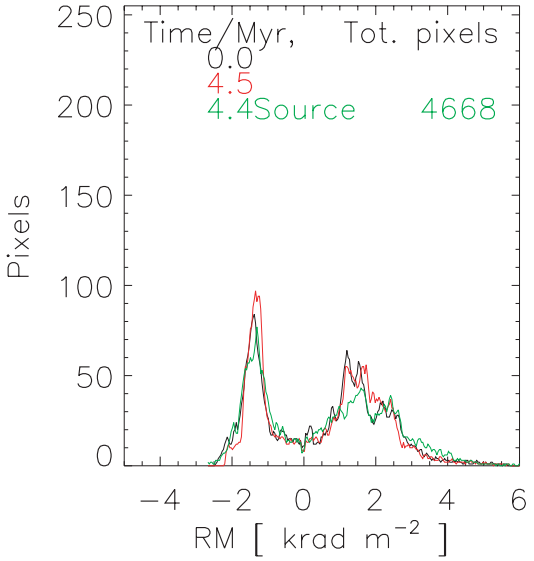

(c) RM histograms of the three maps in (a). Colors are as in panel (b).

Figure 9. Same as Fig. 5 but for the light-fast jets.

faster sources ($v_j \geq 80$ Mach). In agreement, we see that the 'slow' sources cause modest changes on the RM, relative to faster sources. We see that the 'lighter-faster' source, which has the most powerful jets amongst our models, enhances both the mean RM and the RM standard deviation by approximately 70 per cent for a viewing angle of 45° (red curve, Fig. 11, left column). This effect is very important because, as we will discuss in the next section, the observed values of the RM dispersion are used to infer the strength of CMFs. The RM statistics evolution are summarized in Table 2.

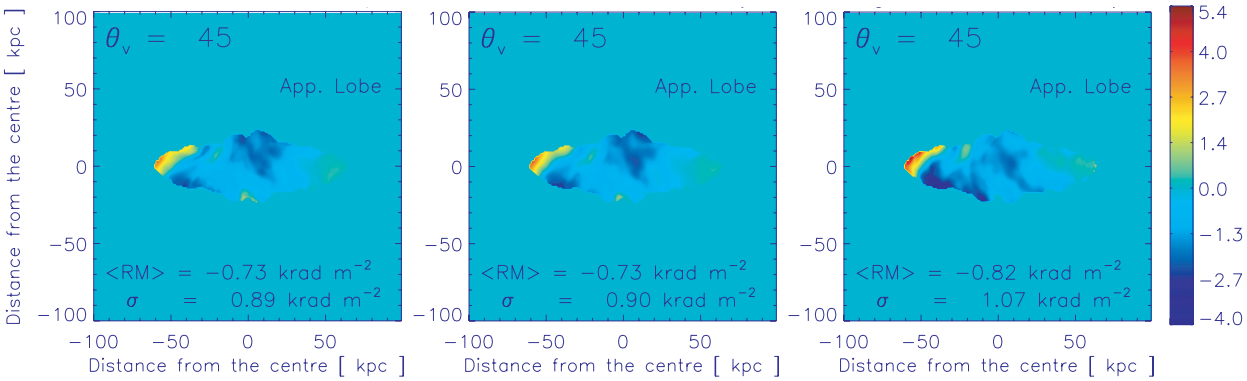

(a) No-source RM map at $t = 0$ Myr (left), No-source RM map at $t = 4.5$ Myr (middle), RM map at $t = 4.4$ Myr (right).

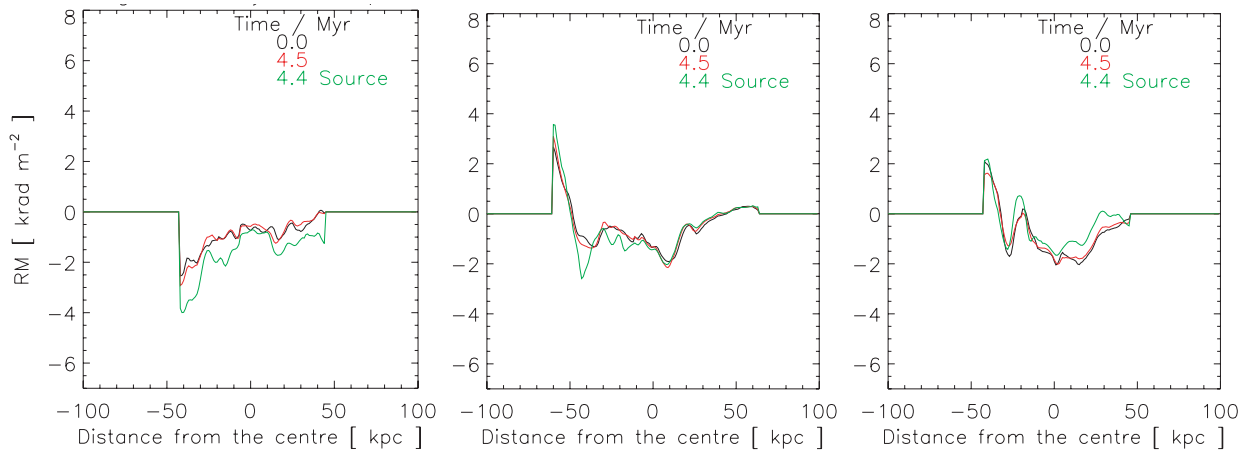

(b) RM at $y = -12$ (left), $y = 0$ (middle) and $y = 12$ kpc (right). The black, red and green curves correspond to the left, the middle and the right panels in (a), respectively.

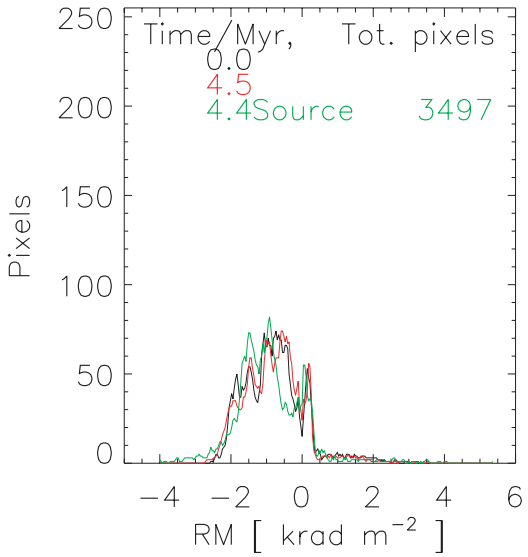

(c) RM histograms of the three maps in (a). Colors are as in panel (b).

Figure 10. Same as Fig. 5 but for the light-fast jets and $\theta_v = 45°$. The approaching lobe is on the positive distance range.

3.4 Field structure evolution

In order to investigate the effects that jets have on the structure of CMFs, we calculate 3D magnetic power spectra in Fourier space using the output from our simulations. Specifically, we use the magnetic fields of the five jets-simulations which were produced at $t = t_e$ (see Table 1). The spectra are shown in Fig. 13(a). For this computation, we exclude the volume that is occupied by the sources (we use the spatial distribution of the jets' tracer; Section 2.4.1).

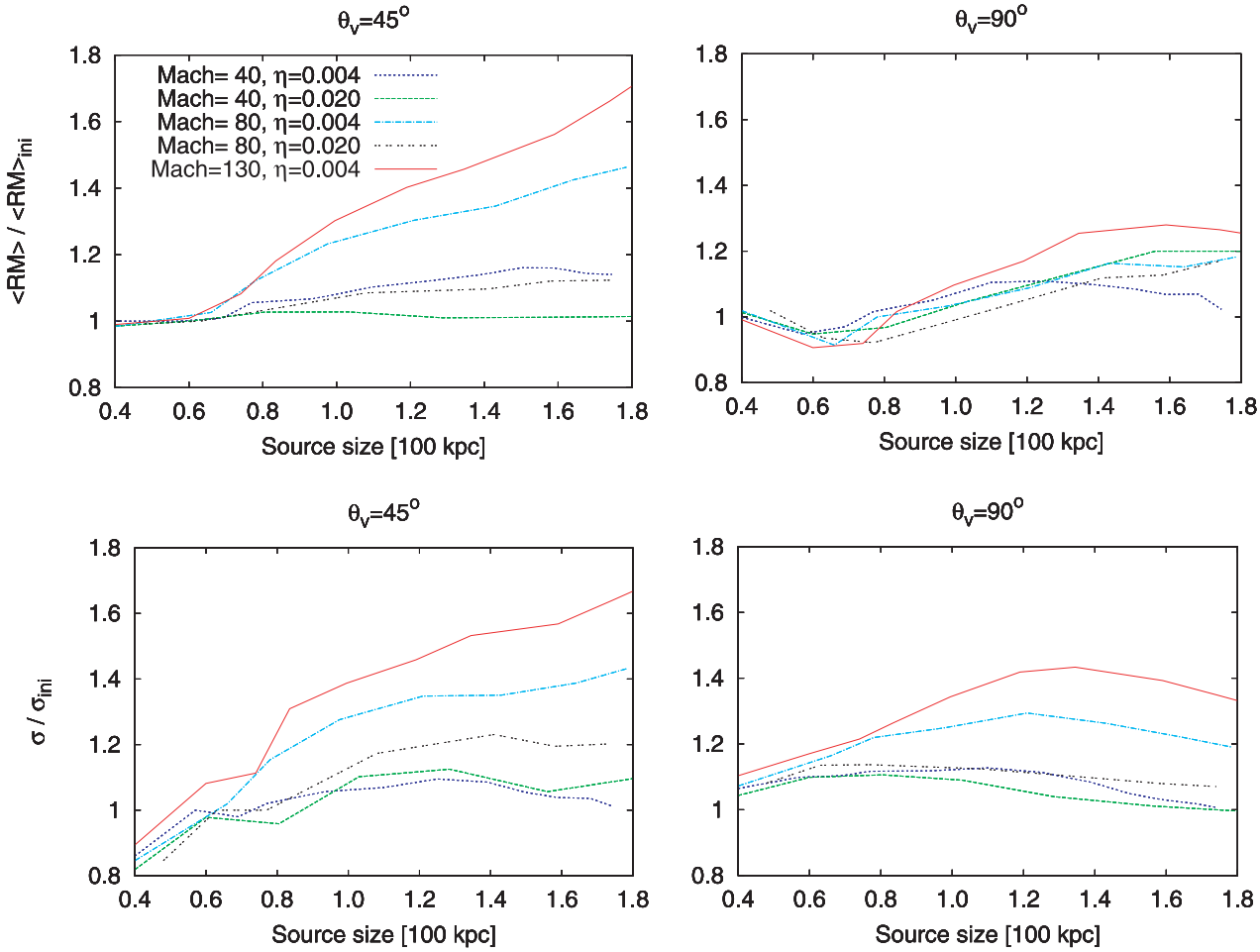

Figure 11. Evolution of the RM statistics as radio sources expand. Panels at the top row display the evolution of the mean RM, whereas panels in the bottom show the evolution of the RM standard deviation. Panels in either the left or the right column correspond to synthetic observations made at 45° or 90°, respectively. The RM is computed using expanding sources at corresponding time-steps. Profiles are normalized to the mean RM, or the RM standard deviation, of corresponding no-source RM maps at $t_{\rm jet} = 0$ (see Section 3.3.1).

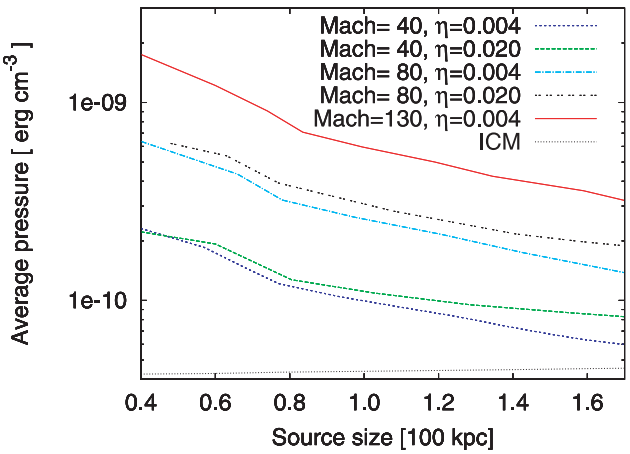

Figure 12. Evolution of the average cocoon thermal pressure as a function of the source size measured from hotspot to hotspot. The ICM thermal pressure is also shown (bottom dashed black line) for reference.

In general, we find that the spectra preserve the initial condition of a power law with a Kolmogorov index (Section 2.3.1). Yet the energy injection from the jets produces power enhancements on scales that range from the resolution limit, 1 kpc, to the source size, ∼40 kpc. An interesting feature that we see is a flattening on the power spectra at the scale defined by the cocoon size – Fig. 13(a). This effect depends on the power of the jets. As radio sources expand, the energy of the jets is transferred to the ICM gas and CMFs in the shocked ambient region. There, magnetic field lines are compressed and stretched tangentially to the surface area of the radio cocoons (Section 3.1). Hence, we find that fatter or more spherical cocoons, such as the ones produced by the 'lighter' jets, are more efficient in increasing and redistributing the energy of the CMFs.

The scales at which the jets affect the CMFs are more evident in Fig. 13(b). There we plot the ratio of the power spectra in Fig. 13(a) over the corresponding spectra computed using the 'no-source' simulation, i.e. for each plot in Fig. 13(b), we use the corresponding profile in Fig. 13(a) as the numerator. The spectrum in the denominator is calculated in the following way. (i) We combine the magnetic fields of the 'no-source' run at $t_{\rm jet} = t_{\rm e}$ with the cocoon spatial distribution of the corresponding jets-simulation at $t_{\rm jet} = t_{\rm e}$. (ii) The magnetic fields inside the cocoon are removed. This yields a cube filled with magnetic fields, which have not been affected by the jets at all, and an empty cavity in the middle. The geometry of such cavity exactly matches the shape and orientation of the cocoon's contact surface. (iii) We compute the 3D magnetic power spectrum of these fields. We note the numerical diffusion of the

Table 2. Summary of the RM statistics evolution. These are the maxima of the mean RM and the RM standard deviation, normalized to their corresponding initial values, reached in synthetic observations that capture the effects of powerful radio sources on CMFs, in terms of the jet power and θ_v.

Simulation	$\max(\langle RM\rangle/\langle RM_{ini}\rangle)$ $\theta_v = 45^\circ$	$\max(\sigma/\sigma_{ini})$ $\theta_v = 45^\circ$	$\max(\langle RM\rangle/\langle RM_{ini}\rangle)$ $\theta_v = 90^\circ$	$\max(\sigma/\sigma_{ini})$ $\theta_v = 90^\circ$
Lighter-slow	1.16	1.09	1.11	1.32
Light-slow	1.03	1.13	1.20	1.11
Lighter-fast	1.46	1.43	1.18	1.29
Light-fast	1.12	1.23	1.17	1.12
Lighter-faster	1.73	1.68	1.28	1.44

simulations is cancelled in the computation of the profiles shown in Fig. 13(b).

Gradients in these spectral ratio profiles persistently show maxima close to 40 kpc, as well as a roughly constant and progressive increase from scales close to 10 kpc down to 1 kpc; see Fig. 13(b). These features are related to the source energy and momentum injection scales and also to the thickness of the ambient medium swept-up region. This gas component expands as the sources evolve towards a thermal pressure equilibrium state with the ICM gas (Fig. 12) and reaches scales of about 10 kpc at the end of the simulations.

We see that the expansion and size of our model cocoons are clearly linked to the enhancement of the CMF power spectra at large scales. The cocoons which are formed by the lightest, fast jets are bigger and have more isotropic gas and energy distributions (see Section 3.2). Fig. 2 illustrates the deformation of the CMFs' topology that is caused by the 'lighter-fast' source at $\theta_v = 90^\circ$ and $t_{jet} = 5.3$ Myr. The cocoon is marked by dots and it clearly stretches and compresses the neighbouring magnetic field lines, particularly ahead of the jets' working surface.

Enßlin & Vogt (2003) have demonstrated that there is a correlation between the statistical properties of the RM distribution, in the real space, and the structure of magnetic fields in the 3D frequency space. Based on these facts, we compute the RM structure functions of those of our synthetic RM maps that correspond to $t_{jet} = t_e$ and $\theta_v = 45^\circ$. The structure function is given by

$$S(\Lambda) = \frac{1}{N(\Lambda)} \sum_{(x,y),(x',y')} [\mathrm{RM}(x, y) - \mathrm{RM}(x', y')]^2, \quad (10)$$

where the sum is taken over the $N(\Lambda)$ non-zero RM pixels that are inside bins (annuli) centred at (x, y) and have radii of $\Lambda = |(x, y) - (x', y')|$ (Simonetti, Cordes & Spangler 1984).

Fig. 13(c) shows the RM structure functions in question. At the end of the simulations, the structure functions generally still show the power law that we have used as the initial conditions of the simulations (Section 2.3.1). Yet these curves considerably flatten at scales of order tens of kpc. The structure functions rise again from a certain scale on. We see that this scale is larger for that sources with fatter cocoons. The flat regions therefore seem to be directly related to the cocoon width. This is consistent with our findings in the 3D magnetic power spectra at the frequency space – Fig. 13(a).

4 DISCUSSION

A combination of 3D MHD numerical simulations and synthetic RM observations have been produced and presented. These simulations follow the evolution and observational signatures of CMFs under the effects of powerful jets from an AGN in the core of a non-cool-core cluster. To understand the basic physics of this interaction, the effects from other cluster galaxies, synchrotron cooling, magnetic reconnections and observational factors (such as beaming, depolarization and light travel effects) have not been considered in the model. We have focused on the role that the jet velocity, the jet density and the observational viewing angle play on the jets–CMFs interaction. Plasma energetics, RM statistics and magnetic power spectra consistently indicate that CMFs are affected by AGN jets. The effect depends on the jets' properties; the lighter and the faster the jets, the more important the results they have on the ambient medium.

The shape of the CMF energetics profiles (Fig. 3) is consistent with the following arguments. Radio sources expand due to the energy injection from jets. The cocoons displace the ICM gas and magnetic fields from the cavity, compressing them into the region located between the contact surface and the bow shock (Figs 1 and 2). These CMF lines are also stretched in this process. The magnetic component tangential to the surface of the radio cocoons is therefore enhanced. As the sources expand, the cocoon pressure decays and the compression caused by bow shocks weakens (Fig. 12). This is in good agreement with radio source evolution models (e.g. see Kaiser & Alexander 1997). Once the sources with Mach 40 jets (green and dark-blue curves, Fig. 12) have expanded for about 100 kpc, their cocoon thermal pressure is comparable with that in the environment. Thus, only these relatively slow sources are not powerful enough to significantly affect the magnetic energy of the ICM.

Our RM integration neglects the contribution from ICM gas and magnetic fields beyond the computational domain. Jet-produced RM enhancements are local, important at the edge of the sources and should not depend on this outer RM component. Observations show that both the cluster ion density and the strength of the CMFs decrease away from the cluster core (Kim et al. 1991; Clarke et al. 2001; Carilli & Taylor 2002, and references therein). Thus, we expect to capture the major contribution to the RM by our procedure. Since the region we use for the analysis is spherical, any additional contribution to the RM is expected to be statistically spatially uniform.

4.1 Characteristic RM gradients

Guidetti et al. (2011) have recently reported bands in the observed RM images of the FR II radio sources 3C 353 and Cygnus A, as well as in the FR I sources 0206+35, M 84 and 3C 270. These bands are perpendicular to the major axis of the radio lobes and are characterized by very little small-scale RM structure. To explain the nature of such features, Guidetti et al. present synthetic RM observations generated with a simple model of gas with constant density and magnetic field distributions. This plasma is then affected by compression induced by an elliptical cavity that is artificially placed

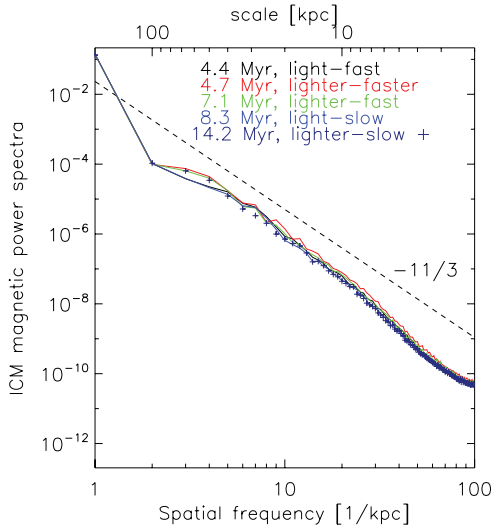

(a) Power spectra for jets with different properties.

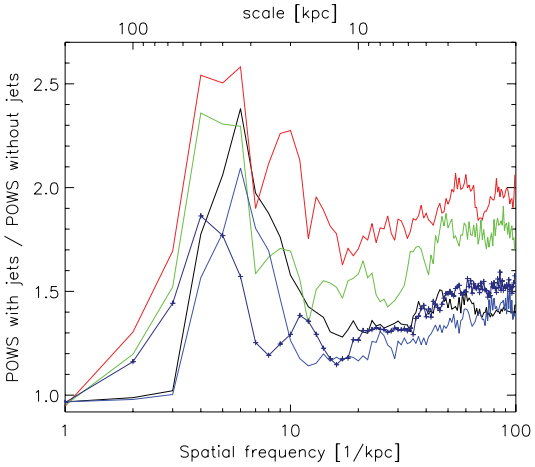

(b) Ratio of the power spectra in (a) over the power spectra of corresponding no-jets simulations (see Section 3.4 for details).

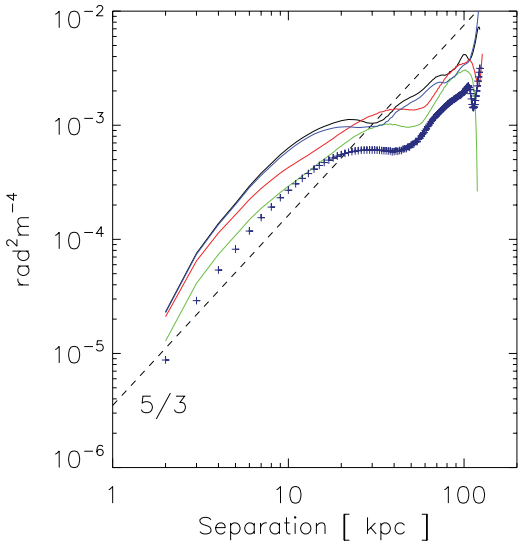

(c) RM structure function produced at $\theta_v = 45°$

Figure 13. Structure of CMFs. (a) and (b) are in the 3D frequency space. (c) is in the 2D scale space of the RM.

inside the gas. The model allows these authors to conclude that there are three magnetic field components associated with observed RM: an isotropic field which has large-scale fluctuations, plausibly associated with the undisturbed ICM; a well-ordered field draped around the leading edges of the radio lobes; a field with small-scale fluctuations which is located in the shells of compressed gas surrounding the inner lobes. We do not use an ordered magnetic field component in our model and do not observe RM bands in our synthetic images. Thus we confirm the findings of Guidetti et al., namely that without any ordered field component in the ICM, the radio source expansion will not lead to banded RM structures.

In addition, our model shows that source-induced RM variations can be as large as 70 per cent, are correlated with the radio jet properties, depend on time and are stronger at the edge of the cocoons. This is a very important point because the observed RM signal is used to infer the strength of the CMFs (e.g. see Feretti et al. 1995, 1999; Taylor et al. 2001; Eilek & Owen 2002).

4.1.1 Asymmetrical RM gradients between radio lobes

Our synthetic RM maps persistently show pronounced gradients at regions corresponding to the receding radio lobes (the left ones) relative to the approaching ones (Figs 5–10). Such RM differences have been observed in the FR IIs Cygnys A (Dreher et al. 1987; Carilli et al. 1994) and 3C 353 (Guidetti et al. 2011) as well as in several FR Is (e.g. 3C 31 and Hydra A, Laing et al. 2008; 3C 449, Guidetti et al. 2010; 0206+53, 3C 270 and M 84, Guidetti et al. 2011). Although we simulate RM enhancements caused by FR II radio sources, FR Is – which are known to form ICM X-ray cavities as well – may well produce similar effects. Hydra A is a well-studied central cluster radio source. The Faraday rotation in this case is thought to be dominated by the local ICM contribution. This cluster presents an ICM magnetic spectral index of $n \approx 11/3$ which has been inferred against the emission from the embedded luminous FR I radio source Hydra A. The inclination angle of this source has been inferred to be within 37°–60° (Taylor & Perley 1993; Enßlin & Vogt 2006; Laing et al. 2008).

In terms of RM statistical fluctuations that are asymmetrical between the source's lobes, we find that our 'lighter-faster' simulation (Table 1) agrees to a certain degree with the studies of Taylor & Perley (1993) and Laing et al. (2008) on Hydra A. This is partly unexpected, as we have chosen a particular realization for the magnetic power spectrum of the CMFs. However, we focus here on the edge effects, which is where we believe that radio sources have the strongest effect: two panels are shown in Fig. 14 where we present curves of $\langle \mathrm{RM} \rangle$ (left-hand panel) and σ_{RM} (right-hand panel) as

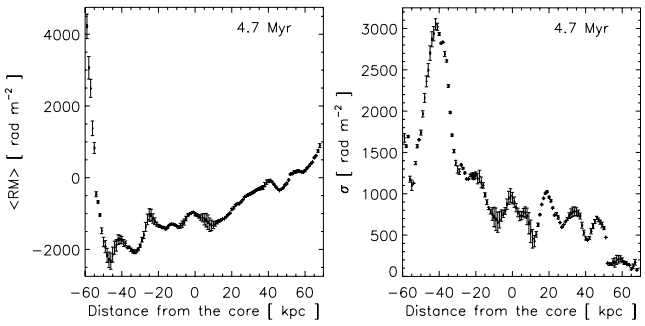

Figure 14. Profiles of RM statistical fluctuation projected on to the jet axis of our 'lighter-faster' source. The viewing angle corresponding to these maps is 45°. The receding lobe is in the negative distance range where fluctuations are the strongest. 20 kpc represent 18.7 arcsec approximately.

a function of position along a horizontal line between the lobes. The mean and standard deviation of the RM are taken on vertical slices of the map corresponding to the 'lighter-faster' simulation at $\theta_v = 45^\circ$ and $t_{jet} = 4.7$ Myr. Vertical error bars are computed by taking the difference between the red and the black curves in Fig. 8. Both statistical measures have large gradients near the left edge. This effect is produced by the expanding radio source. Towards the right edge, the radio source expansion has also strongly amplified the RM values. However, the initial magnetic field in that region happened to be small, which is why this region does not look spectacular. This is quite comparable to the RM distribution in observed radio sources, e.g. see Laing et al. (2008, fig. 22, panels *a* and *b*) who present the RM observations of Hydra A made by Taylor & Perley (1993) along with synthetic RM observation. It is therefore well possible that such large RM gradients towards the edges of radio sources are strongly influenced by the lobe expansion. Note that we consider here only one realization for the random Faraday screen. A detailed match of the considered RM gradient with any observation is therefore not intended.

Our model jets inject energy at scales that range from the resolution limit to the source size, but preferentially near the latter. As we have seen, this results in a flattening in both the magnetic power spectra and the RM structure functions at large scales. Laing et al. (2008), Guidetti et al. (2010) and Guidetti et al. (2011) have reported such flat gradients in the observed structure functions of the FR I sources 3C 31, 3C 270, 3C 449 and Hydra A. Our simulations show that the physics of radio source expansion may explain these structure function gradients naturally. Thus, conclusions about the nature of the ICM turbulence may not be drawn from the gradients in question.

4.1.2 *The Laing–Garrington effect*

We have calculated the mean and the standard deviation of the RM for the approaching ($\langle \mathrm{RM} \rangle^{\mathrm{ap}}$ and $\sigma^{\mathrm{ap}}_{\mathrm{RM}}$) and the receding ($\langle \mathrm{RM} \rangle^{\mathrm{re}}$ and $\sigma^{\mathrm{re}}_{\mathrm{RM}}$) source lobes, as a function of the viewing angle. In the top-left panel of Fig. 15, we show $\langle \mathrm{RM} \rangle^{\mathrm{ap}}$ in solid lines and $\langle \mathrm{RM} \rangle^{\mathrm{re}}$ in dashed lines. In all of these plots, positive (negative) angles correspond to integrations along (against) the line of sight, and again jets are on the plane of the sky at $\pm 90^\circ$. In the bottom-left panel of Fig. 15, we show $\sigma^{\mathrm{re}}_{\mathrm{RM}}/\sigma^{\mathrm{ap}}_{\mathrm{RM}}$. In addition, to demonstrate the effect of the jets on the Faraday screens, which will in turn affect the RM computations, we produce analogous ($\langle \mathrm{RM} \rangle^{\mathrm{re}}$, $\langle \mathrm{RM} \rangle^{\mathrm{ap}}$ and $\sigma^{\mathrm{re}}_{\mathrm{RM}}/\sigma^{\mathrm{ap}}_{\mathrm{RM}}$) plots but use the data from the no-source RM maps (Section 3.3.1). We show these no-source RM plots in the right column of Fig. 15, side by side to their (with) source counterparts.

Together, all of these profiles show that the general dependence of the lobe RM statistics on the viewing angle is shaped by the

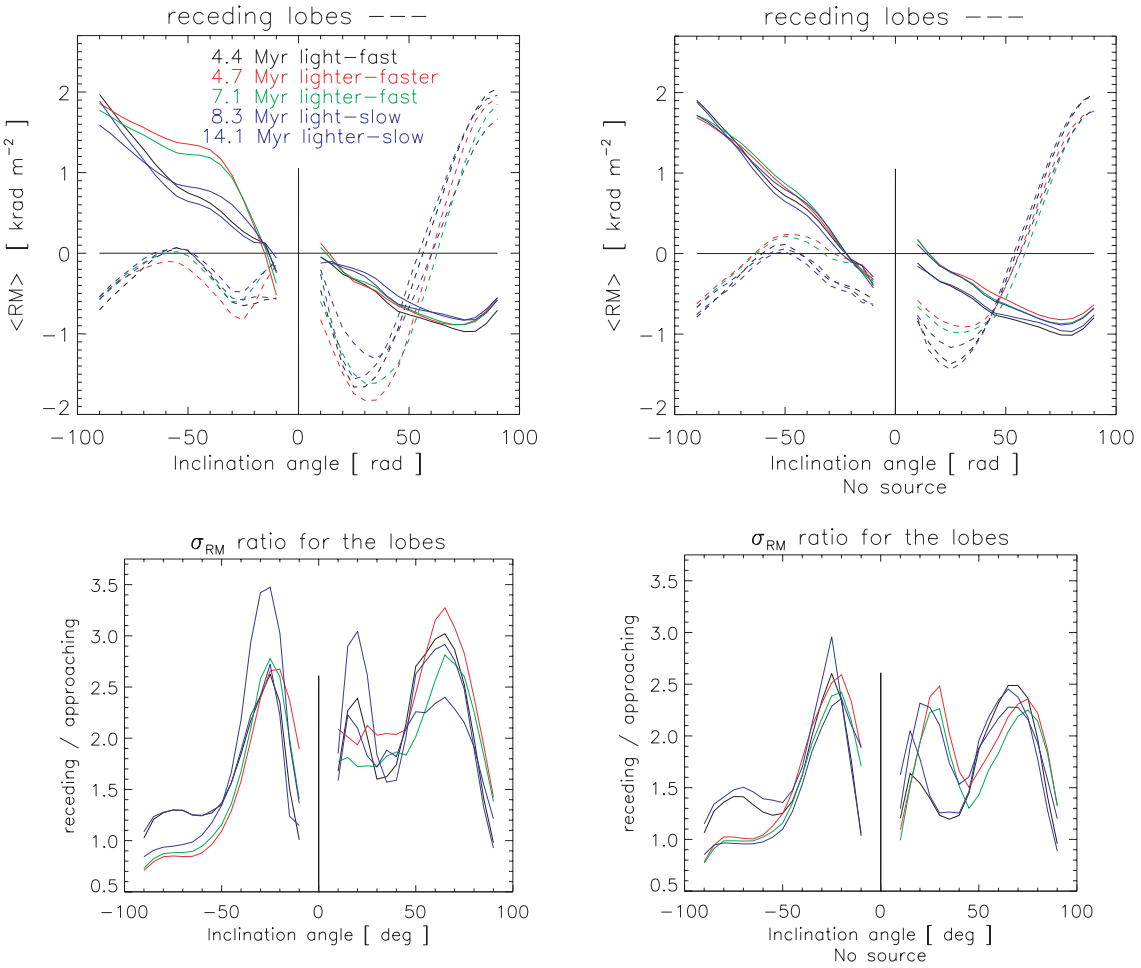

Figure 15. RM statistics comparison between the approaching and receding radio lobes as a function of the angle between the jet axis and the line of sight. Top: mean RM of the approaching (solid) and the receding (dashed) lobes. Bottom: σ_{RM}(receding lobe) /σ_{RM}(approaching lobe). Positive and negative angles represent RM integrations along and against the line of sight, respectively. Panels in the right column show data from no-source RM maps (Section 3.3.1).

intrinsic nature of the Faraday screens, as it is generally assumed in the interpretation of the Laing–Garrington effect. The result of the radio source expansion is to amplify several RM features.

Only for positive inclinations, our realization results in stronger average RMs in the receding lobes (Fig. 15, top panel). We see strong amplification at inclinations of $20^\circ < \theta_v < 70^\circ$. σ_{RM} is linked to the depolarization (Burn 1966; Krause, Alexander & Bolton 2007). Already, intrinsically, the depolarization is always higher for the receding lobe ($\sigma^{re}_{RM}/\sigma^{ap}_{RM} > 1$). Panels in the bottom row (Fig. 15) show that this trend is mostly amplified by the radio sources, apart from the fatter (lighter) ones for which the σ ratio drops below unity near $\theta_v = \pm 90^\circ$. Thus the Laing–Garrington effect is only moderately affected by the radio source expansion, in such a way that the associated trends tend to be amplified.

We have shown that powerful radio sources affect the structure of CMFs which is characterized by the magnetic power spectrum index n. This process is important because the ICM energy transformation, either from or to magnetic form, as well as the observations (Murgia et al. 2004), depend on n. Hence we agree with Laing et al. (2008) in that the structure of CMFs inferred by using the emission of cluster radio sources should take a piecewise-defined form over the range of the spatial frequencies. Our simulations show, moreover, that such functional forms change with time [see Figs 13(a) and (b); note that the profiles in panel (b) would be completely flat otherwise]. Faraday rotation measurements from clusters with broad differences in age will be key in the determination of evolving magnetic structure functions of the CMFs.

5 SUMMARY AND CONCLUSIONS

We have presented a combination of 3D MHD numerical simulations and synthetic RM observations to model the evolution and observational signatures of CMFs under the effects of powerful AGN jets at the core of a non-cool-core galaxy cluster. We prescribe the CMF as a Gaussian random field with a power-law energy spectrum tuned to resemble the expectations for turbulence. We focus on how both the jets' power, in terms of their density and velocity, and the observational angle affect the observed RM signal. Such signal is used by observational studies to infer the strength of CMFs. Our results are very consistent and show the following.

Powerful jets increase the ICM energy in proportion to their velocity and in inverse proportion to their density. Light jets are more efficient in this process because they inflate fatter cocoons than relatively heaver jets. Only jets with Mach numbers of 80 and 130, which are overpressured with respect to the ambient medium, significantly increase the ICM magnetic energy. We see that the time evolution of the CMF energetics is correlated with that of the cocoon pressure.

Jets compress and displace the magnetized ICM. This results in a flattening of the 3D magnetic power spectra and the associated field RM structure functions. This happens at scales from the resolution limit to the source size, but preferentially near the latter. We see the effect is correlated with the jet velocity and pronounced for fat cocoons. The RM structure functions of 3C 31, 3C 270, 3C 449 and Hydra A show flat gradients at large scales, and the cause of such shapes has been previously modelled (Laing et al. 2008; Guidetti et al. 2010, 2011) in terms of ICM turbulence. Our model suggests, however, that the physics of radio source expansion may as well explain this feature.

The general distribution of the Faraday depth is determined by the intrinsic nature of the ICM. Powerful jets enhance the RM locally by factors up to $\sim$1.73. We find this process is proportional to the jet velocity and in inversely proportional to the beam density. Expanding hypersonic sources compress the ICM gas and magnetic fields in the shocked ambient region. The strength of the fields that are perpendicular to the local lobe expansion direction increases, especially near the hotspots. The alignment of compressed CMF components and the line of sight is favoured (i) at the cocoon edge (ii) by sources with a fat cocoon (iii) at θ_v within 20°–70°, due to the cocoon geometry. Jet-produced RM enhancements are thus more important under these conditions and should be more evident in radio galaxies than in quasars.

Both $\langle RM \rangle$ and σ_{RM} continuously change and tend to increase as the radio sources develop. 'Lighter' sources with jet velocities ≥ 40 Mach yield $\langle RM \rangle$ and σ_{RM} enhancement of factors within 1.2–1.7, in proportion to the jet velocity. These RM enhancements may therefore lead to overestimations of the CMF strength by up to about 70 per cent.

ACKNOWLEDGMENTS

It is a pleasure to thank Robert Laing and Malcolm Longair for useful discussions about this paper, as well as the anonymous referee for comments that helped to improve this work. The software used in these investigations was in part developed by the DOE-supported ASC/Alliance Center for Astrophysical Thermonuclear Flashes at the University of Chicago. MH-E acknowledges financial support from CONACyT (the Mexican National Council of Science and Technology, 196898/217314), useful discussions with David Titterington and Jongsoo Kim, Dongwook Lee for the 3D-USM-MHD solver of FLASH 3.1 and Volker Gaibler for the routines to map magnetic field geometry.

REFERENCES

Alexander P., 2002, MNRAS, 335, 610
Alexander P., Leahy J. P., 1987, MNRAS, 225, 1
Allen S. W. et al., 2001, MNRAS, 324, 842
Barthel P. D., 1989, ApJ, 336, 606
Basson J. F., Alexander P., 2003, MNRAS, 339, 353
Batten P., Clarke N., Lambert C., Causon D. M., 1997, SIAM J. Sci. Comput., 18, 1553
Beck R., Brunetti G., Feretti L., 2006, Astron. Nachr., 327, 385
Binney J., Tabor G., 1995, MNRAS, 276, 663
Bîrzan L., McNamara B. R., Nulsen P. E. J., Carilli C. L., Wise M. W., 2008, ApJ, 686, 859
Blanton E. L., Sarazin C. L., McNamara B. R., 2003, ApJ, 585, 227
Boehringer H., Voges W., Fabian A. C., Edge A. C., Neumann D. M., 1993, MNRAS, 264, L25
Bogdanović T., Reynolds C. S., Balbus S. A., Parrish I. J., 2009, ApJ, 704, 211
Bridle A. H., Perley R. A., 1984, ARA&A, 22, 319
Brüggen M., Kaiser C. R., 2002, Nat, 418, 301
Brüggen M., Ruszkowski M., Simionescu A., Hoeft M., Dalla Vecchia C., 2005, ApJ, 631, L21
Burn B. J., 1966, MNRAS, 133, 67
Carilli C. L., Taylor G. B., 2002, ARA&A, 40, 319
Carilli C. L., Perley R. A., Harris D. E., 1994, MNRAS, 270, 173
Churazov E., Brüggen M., Kaiser C. R., Böhringer H., Forman W., 2001, ApJ, 554, 261
Clarke D. A., Harris D. E., Carilli C. L., 1997, MNRAS, 284, 981
Clarke T. E., Kronberg P. P., Böhringer H., 2001, ApJ, 547, L111
Dolag K., Bartelmann M., Lesch H., 2002, A&A, 387, 383
Dreher J. W., Carilli C. L., Perley R. A., 1987, ApJ, 316, 611
Dubois Y., Teyssier R., 2008, A&A, 482, L13
Eilek J. A., Owen F. N., 2002, ApJ, 567, 202
Enßlin T. A., Vogt C., 2003, A&A, 401, 835

Enßlin T. A., Vogt C., 2006, A&A, 453, 447
Fanaroff B. L., Riley J. M., 1974, MNRAS, 167, 31
Feretti L., Giovannini G., 2008, Lecture Notes in Physics, Vol. 740, Clusters of Galaxies in the Radio: Relativistic Plasma and ICM/Radio Galaxy Interaction Processes. Springer, Berlin, p. 143
Feretti L., Dallacasa D., Giovannini G., Tagliani A., 1995, A&A, 302, 680
Feretti L., Dallacasa D., Govoni F., Giovannini G., Taylor G. B., Klein U., 1999, A&A, 344, 472
Fryxell B. et al., 2000, ApJS, 131, 273
Garrington S. T., Leahy J. P., Conway R. G., Laing R. A., 1988, Nat, 331, 147
Ge J. P., Owen F. N., 1993, AJ, 105, 778
Govoni F., Murgia M., Feretti L., Giovannini G., Dolag K., Taylor G. B., 2006, A&A, 460, 425
Guidetti D., Murgia M., Govoni F., Parma P., Gregorini L., de Ruiter H. R., Cameron R. A., Fanti R., 2008, A&A, 483, 699
Guidetti D., Laing R. A., Murgia M., Govoni F., Gregorini L., Parma P., 2010, A&A, 514, A50
Guidetti D., Laing R. A., Bridle A. H., Parma P., Gregorini L., 2011, MNRAS, 413, 2525
Heinz S., Reynolds C. S., Begelman M. C., 1998, ApJ, 501, 126
Huarte-Espinosa M., Alexander P., Bolton R., Geisbuesch J., Krause M., 2009, Rev. Mex. Astron. Astrofis., 36, 231
Huarte-Espinosa M., Krause M., Alexander P., 2011, MNRAS, 417, 382 (Paper I)
Jones T. W., 2008, in Rector T. A., De Young D. S., eds, ASP Conf. Ser. Vol. 386, The Role of MHD in the ICM and its Interactions with AGN Outflows. Astron. Soc. Pac., San Francisco, p. 398
Kaiser C. R., Alexander P., 1997, MNRAS, 286, 215
Kaiser C. R., Alexander P., 1999, MNRAS, 305, 707
Kim K.-T., Kronberg P. P., Tribble P. C., 1991, ApJ, 379, 80
King I. R., 1972, ApJ, 174, L123
Krause M., 2003, A&A, 398, 113
Krause M., 2005, A&A, 431, 45
Krause M., Alexander P., Bolton R., 2007, in Proceedings of Science, From Planets to Dark Energy: the Modern Radio Universe. Univ. Manchester, Manchester, p. 109 (http://pos.sissa.it/)
Krause M., Alexander P., Bolton R., Geisbuesch J., Green D. A., Riley J., 2009, MNRAS, 400, 646
Laing R. A., 1988, Nat, 331, 149
Laing R. A., Bridle A. H., Parma P., Murgia M., 2008, MNRAS, 391, 521
Lee D., Deaane A. E., 2008, J. Comput. Phys., 228, 952
McNamara B. R. et al., 2000, ApJ, 534, L135
McNamara B. R., Nulsen P. E. J., Wise M. W., Rafferty D. A., Carilli C., Sarazin C. L., Blanton E. L., 2005, Nat, 433, 45
Murgia M., Govoni F., Feretti L., Giovannini G., Dallacasa D., Fanti R., Taylor G. B., Dolag K., 2004, A&A, 424, 429
Nulsen P. E. J., David L. P., McNamara B. R., Jones C., Forman W. R., Wise M., 2002, ApJ, 568, 163
Nulsen P. E. J., McNamara B. R., Wise M. W., David L. P., 2005, ApJ, 628, 629
Omma H., Binney J., Bryan G., Slyz A., 2004, MNRAS, 348, 1105
Press W. H., Teukolsky S. A., Vetterling W. T., Flannery B. P., 1992, in Press W. H., Teukolsky S. A., Vetterling W. T., Flannery B. P., eds, Numerical Recipes in FORTRAN. The Art of Scientific Computing. Cambridge Univ. Press, Cambridge
Quilis V., Bower R. G., Balogh M. L., 2001, MNRAS, 328, 1091
Reynolds C. S., Heinz S., Begelman M. C., 2001, ApJ, 549, L179
Roettiger K., Stone J. M., Burns J. O., 1999, ApJ, 518, 594
Rudnick L., Blundell K. M., 2004, in Reiprich T., Kempner J., Soker N., eds, The Riddle of Cooling Flows in Galaxies and Clusters of Galaxies. Available at: http://www.astro.virginia.edu/coolflow/
Ruszkowski M., Enßlin T. A., Brüggen M., Heinz S., Pfrommer C., 2007, MNRAS, 378, 662
Ruzmaikin A., Sokolov D., Shukurov A., 1989, MNRAS, 241, 1
Ryu D., Kang H., Cho J., Das S., 2008, Sci, 320, 909
Schekochihin A. A., Cowley S. C., Taylor S. F., Maron J. L., McWilliams J. C., 2004, ApJ, 612, 276
Schekochihin A. A., Cowley S. C., Kulsrud R. M., Hammett G. W., Sharma P., 2005, ApJ, 629, 139
Scheuer P. A. G., 1974, MNRAS, 166, 513
Schindler S., 2002, in Ferotti L., Gioia I. M., Giovanni G., eds, Astrophysics and Space Science Library, Vol. 272, Merging Processes in Galaxy Clusters. Astrophysics and Space Science Library, p. 229
Schmidt R. W., Fabian A. C., Sanders J. S., 2002, MNRAS, 337, 71
Simonetti J. H., Cordes J. M., Spangler S. R., 1984, ApJ, 284, 126
Smith D. A., Wilson A. S., Arnaud K. A., Terashima Y., Young A. J., 2002, ApJ, 565, 195
Soker N., Sarazin C. L., 1990, ApJ, 348, 73
Taylor G. B., Perley R. A., 1993, ApJ, 416, 554
Taylor G. B., Govoni F., Allen S. W., Fabian A. C., 2001, MNRAS, 326, 2
Tribble P. C., 1991, MNRAS, 253, 147
Vogt C., Enßlin T. A., 2003, A&A, 412, 373
Vogt C., Enßlin T. A., 2005, A&A, 434, 67
Xu H., Li H., Collins D. C., Li S., Norman M. L., 2010, ApJ, 725, 2152

This paper has been typeset from a TEX/LATEX file prepared by the author.